Numerical investigation on the heat transfer in wind turbulence over breaking waves

Min Lu ⬤, Zixuan Yang ⬤,* and Guowei He

*Institute of Mechanics, Chinese Academy of Sciences, Beijing 100190, People's Republic of China
and School of Engineering Sciences, University of Chinese Academy of Sciences,
Beijing 101408, People's Republic of China*

Lian Shen ⬤

*Department of Mechanical Engineering & St. Anthony Falls Laboratory, University of Minnesota,
Minneapolis, Minnesota 55455, USA*

Heat transfer in wind turbulence over breaking waves is studied through direct numerical simulations. The air-water system is simulated on an Eulerian grid with the interface between the two phases captured by a coupled level set and volume-of-fluid method. To examine the effect of wave age, different cases representing slow, intermediate, and fast waves are considered for the scenario of air temperature being higher than the water temperature. The results show that the evolution of mean temperature profile responds nonmonotonically to the increasing wave age. At a small wave age, the mean temperature near the water surface increases after wave breaking. At intermediate and large wave ages, however, the temperature decreases after wave breaking, while the decrement magnitude is larger at the intermediate wave age. An investigation of the temperature fluctuation flux indicates that a combined effect of wave-coherent flux and turbulence-induced flux leads to a large magnitude of temperature decrement at the intermediate wave age. A further analysis of the production term in the transport equation of the turbulence-induced temperature flux elucidates the mechanism underlying the generation of the turbulence-induced flux at the intermediate wave age. The findings of the present study suggest that temperature responds in a more complex manner to wave age than velocity does and this phenomenon should be considered in models for air-sea interaction and weather forecasting.

I. INTRODUCTION

Heat transfer between the oceans and atmosphere plays a vital role in weather and climate change. The interaction between wind and water waves alters the structure of airflow over waves [1–3], which further impacts the heat transfer [4–6]. Due to the coupling between momentum and heat transfer, deviations of the predicted results from field observations occur when the air-sea interaction is not taken into account properly in weather prediction models [7–10]. Wave breaking is recognized as one of the most violent air-sea interaction processes. It strongly enhances the heat, mass, and momentum transfer between the oceans and atmosphere [4,11–13]. Understanding the mechanism of heat transfer in wind turbulence over breaking waves is crucial for improving marine numerical weather forecasting models.

---

*Contact author: yangzx@imech.ac.cn

The research on wave breaking has a long history and the corresponding flow physics have been understood from different aspects [14]. The geometry of breaking waves has been one of the focuses of laboratory experiments [15–19]. The limiting wave steepness associated with the occurrence of wave breaking, the shape of wave crests, and the surface-elevation profile were measured to characterize the geometry of breaking waves [20]. Laboratory experiments were also conducted to investigate the onset criteria of wave breaking [21,22], which can be classified into geometric [23,24], kinematic [25,26], and dynamic breaking criteria [27–31]. Another intriguing topic is the energy dissipation caused by wave breaking. Investigations in the literature focused on the estimation of total dissipation [32,33] and spectral distribution of the energy dissipation [23,34,35].

Enabled by the advancement in computer power and robust multiphase flow solvers, high-fidelity simulations of wave breaking were conducted [36–41]. Many previous studies validated the capability of numerical simulation by reproducing the postbreaking features obtained from laboratory experiments and investigated the turbulence quantities of the flow fields. For example, a numerical study on the wind turbulence modulated by wave breaking was conducted by Yang *et al.* [39]. They found that the kinetic energy of wind velocity fluctuations was enhanced during the wave breaking in both the slow and fast wave cases, whereas such a transient enhancement of the airflow kinetic energy was not observed in the intermediate wave cases. While Yang *et al.* [39] showed the impact of wave age on the wind velocity field above breaking waves, the transport of air temperature was not studied.

Heat exchange across gas-liquid interfaces has been studied through both field observations [42–46] and laboratory experiments [2,9,47]. In early works, bulk formula parametrization models for air-sea heat exchange were proposed to calculate the heat transfer coefficient, in which the wind speed and the temperature difference between air and water were regarded as the dominant factors. The surface motions were not considered, and thus the interaction between the airflow and propagating waves was neglected in the early models [43,48,49]. Later, it was reported that the sea surface temperature and wind power input were significantly modified when the interaction between the airflow and waves was considered in the weak-wind regime [7,50]. In the low- to intermediate-wind regime, it was reported that the microscale wave breaking induced turbulence and thus became an important mechanism contributing to air-water heat transfer [6]. In the high-wind regime, it was suggested that the mechanism for the ratio of the heat transfer coefficient to the surface friction coefficient is governed by the existence of wave breaking and spray [2].

Numerical simulations were also conducted to provide insights into the heat transfer in turbulent flows of various types of interface geometries. Many works focused on the heat transfer over stationary flat and wavy walls. It was discovered that coherent flow structures dominating the dynamics of turbulence also imposed significant impacts on the heat transfer [51–53]. As a result, the temperature fluctuation was found to be highly correlated with the streamwise velocity fluctuation, particularly in the near-wall region [54–57]. In the investigations of scalar transport over wavy walls, it was observed that streamwise vortices induced both sweeplike and ejectionlike motions to affect the heat fluxes in the near-wall region [58–60]. When the steepness of the wavy wall is small, an increase in the wave steepness intensifies streamwise vortices, resulting in an enhancement of heat fluxes [58]. However, as the wave steepness exceeds a critical value, heat fluxes are not further enhanced [61,62].

In the wind-wave coupling system, it is well understood that the wave motion imposes notable influences on the airflow and thus modifies the flow structures [63–68]. As such, numerical simulations were also conducted to study the scalar transport with wavy and mobile boundaries, among which some focused on the water side [69–72]. More relevant to the present study, Yang and Shen [66] performed single-phase direct numerical simulation (DNS) of the scalar transport in air over prescribed progressive surface waves. They reported significant effects of wave age on scalar transport. The strong wave-phase-dependent characteristics of instantaneous scalar fluctuations and fluxes were also emphasized in their study. Lakehal *et al.* [73] conducted two-phase simulations to study the impact of interface dynamics on the heat transfer in air. They pointed out that the free

surface led to a stronger vertical turbulent heat flux than the rigid wall, because the mobile surface enhanced the vertical velocity fluctuation. To limit the wave steepness, they considered a situation with large surface tension, and as such the wave remained steady without breaking.

From the above review of previous studies of heat transfer over static and mobile surfaces, it is understood that the heat transfer process is highly correlated with the interface dynamics. It can be anticipated that the air-sea interaction during wave breaking imposes complex influences on the temperature field in wind turbulence. Despite its importance, this research topic has not been studied adequately in the literature. This is because the heat transfer over breaking waves is complex, as it involves multiple processes such as interface topology change, bubble dissolution, and droplet evaporation [74–78]. It is challenging to analyze all of these processes because of their multiscale properties. The objective of our study is to analyze sensible heat transfer in the air flowing over breaking waves, with a focus on the impact of interface topology change. We note that the bubbles and droplets created by the wave-breaking process are captured in our simulation, while the effects of bubble dissolution and droplet evaporation are neglected. This is because a well-resolved droplet needs more than 20 grid points per diameter [79], which is infeasible in a DNS of wave breaking with the current computing power. Thus, we are not attempting to capture the small-scale phase-change process in our present paper. This approach is reasonable because the phase change happens in the evaporation layer [78], which is away from the near-wave region of our interests. In the near-wave region, the already humid air mitigates further droplet evaporation, making the latent heat effect subtle compared to sensible heat transfer during wave breaking. As such, the present study can serve as the first step towards understanding the effect of interface topology change on overall heat transfer.

In the present study, the wave age effect is particularly emphasized by performing various cases as representations of the young, intermediate, and old wave conditions. To ensure the convergence of the calculation of turbulence statistics, each case is run repeatedly for 100 times, with the initial instantaneous velocity and temperature fluctuations varying among different runs. Ensemble averaging over different runs is then used to define turbulence statistics, including the mean temperature, temperature fluctuation fluxes, and the budget terms in the corresponding transport equations. The analyses start with the evolution of plane-averaged temperature and are gradually refined by examining the heat transfer process. The mechanism underlying the heat transfer induced by the wave and turbulent motions is further investigated through temperature fluxes and the production terms in their transport equations.

In the remainder of this paper, the numerical methods are introduced in Sec. II. The configurations of the simulation are given in Sec. III. The numerical results are discussed in Sec. IV, followed by conclusions in Sec. V.

II. NUMERICAL METHOD

In the present study, we investigate the heat transfer in wind turbulence over breaking waves through DNS. The computational domain is shown in Fig. 1. The Cartesian coordinates are denoted by x, y, and z in the streamwise, spanwise, and vertical directions, respectively. The size of the computational domain is $L_x \times L_y \times L_z = 2\lambda \times 1.5\lambda \times 2.5\lambda$, where λ is the wavelength. The mean water depth is $d = 0.5\lambda$ and the mean height of air is $h = 2\lambda$. The mean water level is set to $z = 0$. The airflow is driven by a constant shear stress τ in the streamwise direction at the top of the computational domain, while the free-slip boundary condition is imposed at the bottom of the water. Temperature in deep water and in air far away from the air-sea interface is unlikely to be changed during the short period of wave breaking and thus a Dirichlet boundary condition of $\theta = 1$ at the upper boundary and $\theta = 0$ at the lower boundary is prescribed for the temperature field. The periodic boundary condition is applied for both the temperature and velocity fields in the horizontal directions. The number of grid points is $N_x \times N_y \times N_z = 320 \times 192 \times 360$. The computational domain is discretized evenly in both the x and y directions, and the grid is refined near the wave surface in the z direction, with the finest resolution $\Delta_z = 0.002\lambda$.
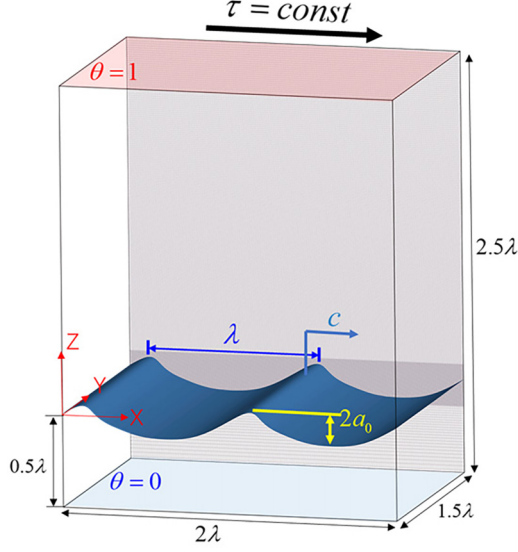
FIG. 1. Schematic diagram of the numerical simulation configuration. The flow is driven by a constant shear stress applied at the top of the computational domain. Initially, a water wave propagates in the x direction with a phase speed c. The wavelength is λ and the amplitude is a_0. The temperature at the top and bottom boundaries is set to be $\theta = 1$ and $\theta = 0$, respectively.

The two-fluid flows are governed by a single set of equations. The continuity and momentum equations are written as

$$\nabla \cdot \mathbf{u} = 0, \tag{1}$$

$$\frac{\partial(\rho \mathbf{u})}{\partial t} + \nabla \cdot (\rho \mathbf{u}\mathbf{u}) = -\nabla p + \nabla \cdot (2\mu \mathbf{S}) + \rho \mathbf{g} + \sigma \kappa \nabla H(\phi). \tag{2}$$

Here, t is time; $\mathbf{u}$ is the velocity vector; ρ and μ are the fluid density and viscosity, respectively; p is the pressure; $\mathbf{S}$ is the strain-rate tensor; $\mathbf{g}$ is the gravitational acceleration; σ is the surface tension coefficient; κ is twice the mean curvature of the interface; and $H(\phi)$ is the Heaviside function, defined as

$$H(\phi) = \begin{cases} 0, & \phi \leqslant 0 \\ 1, & \phi > 0, \end{cases} \tag{3}$$

where ϕ is the level-set (LS) function with $\phi = 0$ representing the air-water interface. The evolution of temperature is governed by the following advection-diffusion equation:

$$\frac{\partial(\rho c_p \theta)}{\partial t} + \nabla \cdot (\rho c_p \theta \mathbf{u}) = \nabla \cdot (D \nabla \theta), \tag{4}$$

where θ is the temperature, c_p is the specific heat capacity, and D represents the thermal conductivity coefficient. Because the characteristic timescale of wave breaking is short in comparison with the buoyancy effect, we consider a neutrally stratified condition, and the phase change is not included. In other words, the temperature is treated as a passive scalar.

In numerical simulations of two-fluid flows with a large density ratio and a high volumetric heat capacity ratio, the discontinuity of physical properties at the interface may cause numerical instability. To ensure numerical robustness, an anticipation-correction strategy is adopted to evolve

the density ρ and volumetric heat capacity ρc_p. In the correction step, the following transport equations of ρ and ρc_p are evolved [80,81]:

$$\frac{\partial \rho}{\partial t} + \nabla \cdot (\rho \mathbf{u}) = 0, \tag{5}$$

$$\frac{\partial (\rho c_p)}{\partial t} + \nabla \cdot (\rho c_p \mathbf{u}) = 0. \tag{6}$$

Equations (5) and (6) are solved using the same time-integration and spatial-discretization schemes as the momentum and heat transfer equations [i.e., Eqs. (2) and (4)]. Specifically, these equations are all advanced using the second-order Runge-Kutta (RK2) method, and the convection terms are all spatially discretized using a third-order cubic upwind interpolation (CUI) scheme. The diffusion terms in Eqs. (2) and (4) are discretized using a second-order central difference scheme. The divergence-free condition given by Eq. (1) is satisfied by applying a fraction-step method. In the correction step, the air-water interface is captured using the coupled level set and volume-of-fluid (CLSVOF) method, which solves the following transport equations of both the LS and volume-of-fluid (VOF) functions [82,83]:

$$\frac{\partial \phi}{\partial t} + \nabla \cdot (\phi \mathbf{u}) = 0, \tag{7}$$

$$\frac{\partial \varphi}{\partial t} + \nabla \cdot (\varphi \mathbf{u}) = 0, \tag{8}$$

where φ denotes the VOF function. In the CLSVOF method, a piecewise linear interface is reconstructed in each grid cell to calculate the flux of the VOF function. The interface normal direction is calculated using the LS function, while its distance from the cell center is determined by the VOF function. As such, the flux of VOF is calculated accurately. The VOF function ensures mass conservation of each phase of the fluids. The reconstructed interface is used to reinitialize the LS function, such that the LS function keeps the property of a distance function near the interface. After the evolution of the LS and VOF functions, the physical properties are corrected using the LS function as

$$\chi = H(\phi)\chi_w + [1 - H(\phi)]\chi_a, \tag{9}$$

where χ represents the physical properties, and the subscripts "a" and "w" denote air and water, respectively. The validation of the flow solver is given in detail in Ref. [80]. In close relevance to the present study, the simulation results of wave breaking without wind show good agreement with previous studies [80]. Lu *et al.* [81] validated the temperature solver in various test cases, among which the evolution of temperature field during wave breaking shows that the solver is robust for simulating heat transfer in two-fluid flows with high contrast of the volumetric heat capacity between air and water.

III. SIMULATION DETAILS

A. Initialization of flow and temperature fields

Following the initialization strategy of velocity field proposed by Yang *et al.* [39], the wind turbulence and temperature fields are initially generated by enforcing the wave geometry unchanged till the wind turbulence is fully developed. The initial elevation of the wave is given by the following analytical solution of a Stokes wave as

$$\eta(x) = a_0 \cos(kx - \omega t) + \frac{\varepsilon_0 a_0}{2} \cos[2(kx - \omega t)] + \frac{3\varepsilon_0^2 a_0}{8} \cos[3(kx - \omega t)], \tag{10}$$

where η is the surface elevation, a_0 is the initial amplitude of the wave component, $\varepsilon_0 = ka_0$ is the initial linear wave steepness, $k = 2\pi/\lambda$ is the angular wave number, and $\omega = \sqrt{gk(1 + \varepsilon_0^2)}$ is the angular frequency. In the water, the initial velocity is given based on the potential flow theory [84],

TABLE I. Computational parameters for heat transfer in wind over breaking waves.

Case	ε_0	c/u_*	Re_τ	ρ_a/ρ_w	μ_a/μ_w	Pr	α_a/α_w
1	0.55	3.7	180	0.0012	0.0154	0.71	128.3
2	0.55	8.0	180	0.0012	0.0154	0.71	128.3
3	0.55	12.0	180	0.0012	0.0154	0.71	128.3
4	0.55	20.0	180	0.0012	0.0154	0.71	128.3
5	0.55	27.7	180	0.0012	0.0154	0.71	128.3

and thus the free-slip boundary at the bottom wall imposes no effect on the prescribed water velocity before the wave-breaking simulation starts. The temperature in water is prescribed as $\theta = 0$. The temperature in air is initially set as a linear function of elevation and evolves along with the air motion. After the turbulent velocity and temperature fields in the air are fully developed, we store the data at different time instants and set them as the initial conditions of different ensemble runs for the follow-up wave-breaking simulations.

B. Simulation parameters

Key parameters of the present simulations are listed in Table I. In all cases, the initial wave steepness is set to $\varepsilon_0 = 0.55$ to generate breaking waves. According to many previous studies [23,24,85,86], wave breaking occurs at approximately $\varepsilon_0 = 0.35$. As the initial wave steepness increases, the breaking process becomes increasingly strong, and as such the wave breaking imposes a more significant effect on the momentum transfer in the airflow [39,87]. In a deep-water condition, the wave steepness is limited because of wave breaking. A Stokes wave with $\varepsilon_0 = 0.55$ may not exist in deep-water conditions, unless waves with different wavelengths focus together. However, it is computationally expensive to reproduce the complete process that a breaking wave is induced in numerical simulation. Instead, it is a common practice to prescribe a steep wave as the initial condition to perform mechanistic studies [37–41,87]. The main focus of this paper is to shed light on the heat transfer under the effect of interface topology change. Therefore, we follow the convention in the literature to prescribe steep initial waves with $\varepsilon_0 = 0.55$ to generate a violent breaking. In accordance with the previous research by Yang and Shen [64], it has been emphasized that the wave age effect significantly influences the contribution of wave motion to turbulence fluxes. In the present study, we investigate five different wave ages, namely, $c/u_* = 3.7, 8.0, 12.0, 20.0$, and 27.7, to explore the effect of wave age on heat transfer during the wave-breaking process. These wave ages span three key stages of wind-wave interaction: slow waves, intermediate waves, and fast waves. The phase speed c is defined as the ratio between the angular frequency ω and wave number k of the initial prescribed wave, and $u_* = \sqrt{(\tau/\rho_a)}$ is the friction velocity of wind turbulence. In the real atmosphere-ocean system, the friction Reynolds number $\mathrm{Re}_\tau = u_*\lambda/\nu_a$ is $O(10^5–10^6)$, which is far beyond the capability of the computing power at present to conduct DNS. Thus, Re_τ in the present study is reduced to 180. We note that large-scale and very large-scale motions exist in the outer layer of air turbulence with high Reynolds numbers. These large-scale motions impose significant effects on the inner layer, modulating the coherent structures [88–91]. However, reducing the Reynolds number in the present study is justified because the large-scale motions impose limited impacts on the turbulent active region ($y^+ \approx 30$), which is the focus of our present study. Additionally, the effect of Reynolds number on the breaking process is relatively small compared to the effect of wave steepness, as reported in many previous studies [38,92–95]. Therefore, the reduction of the Reynolds number should not undermine the main conclusions. Other flow parameters in the present study are the same as in Ref. [39], including the ratios of density, ρ_a/ρ_w, and dynamic viscosity, μ_a/μ_w, between air and water. The wave Reynolds number $\mathrm{Re}_w = \mathrm{Re}_\tau \nu_a c/(\nu_w u^*)$ is employed in our simulation to relate the friction Reynolds number Re_τ to the wave age c/u^*. Thus, the wave age effect is accounted for in our simulation through different wave Reynolds numbers.

For the simulation of the temperature field, the Prandtl number $\text{Pr} = \nu_a/\alpha_a$ in the air is 0.71, where $\alpha = D/\rho c_p$ is the thermal diffusivity. The ratio of the thermal diffusivity between air and water, α_a/α_w, is 128.3. In the present study, we focus on heat transfer in the air phase. The Batchelor scale in the air phase $\eta_B = \eta_K \text{Pr}^{-0.5}$ is 1.195 times the Kolmogorov scale η_K, indicating that the grid resolution is also sufficient to resolve the temperature field in the air phase. In the water phase, the Batchelor scale is smaller than the Kolmogorov scale because of a larger value of the Prandtl number ($\text{Pr} = 7.1$) in water, which means that the resolution adopted by Yang *et al.* [39] is insufficient to resolve small-scale temperature fluctuations in the water phase. Nevertheless, to reduce computational costs, we do not refine the resolution in the water phase, although we solve for the temperature in water. This choice is necessitated by the limitation in computing power and can be justified by the fact that the temperature inside the water is fixed at zero before the wave-breaking simulation begins, and the specific heat capacity in the water phase is large. As a result, the temperature in the water remains nearly constant throughout the simulation. Additionally, because temperature is treated as a passive scalar, it does not affect the wave geometries. Thus, the underresolved temperature inside the water phase has a minimal impact on wind turbulence and heat transfer in the air domain.

It is noteworthy to mention that the simulations in our study are computationally intensive and time consuming. This is due to the high unsteadiness in the flow and temperature fields caused by wave breaking, which cannot be captured by turbulent statistics based on time averaging. To generate the initial field before wave breaking, each wave age case requires approximately five weeks to develop a fully turbulent wind field, utilizing 1536 cores for parallel computing. Subsequently, 100 runs are conducted for each wave age case (500 runs in total), with each run averaging one day of computational time using 1536 cores. This constrains our ability to conduct a broader parameter sweep given the current computational resources. Nevertheless, the results presented in this paper still provide primary insights into heat transfer over breaking waves, particularly regarding the wave age effect.

C. Definition of turbulent statistics

We conduct 100 runs for each wave age case and calculate the ensemble averaging over the runs to define turbulent statistics. The initial wave geometry for different runs remains the same, while the instantaneous velocity and temperature fluctuations are different because they are chosen from different time instants of a statistically stationary flow field. At the start of each run, the time is set as $t = 0$. The simulation is stopped at $t = 3T$ when the wave breaking calms down. Here, $T = 2\pi/\omega$ is the period of the wave.

Following Yang *et al.* [39], an overbar is used to define a phase-averaged quantity $\bar{f}(x, z, t)$. The phase averaging is performed in the spanwise direction over different runs for a specific wave phase, and as such it is a function of the streamwise coordinate x, vertical coordinate z, and time t. The fluctuations with respect to the phase averaging are defined as

$$f'' = f - \bar{f}. \tag{11}$$

The phase-averaged quantity $\bar{f}$ can be further decomposed into a plane-averaged part $\langle f \rangle (z, t)$ and a wave-coherent part $\tilde{f}(x, z, t)$ as

$$\bar{f} = \langle f \rangle + \tilde{f}. \tag{12}$$

The fluctuation with respect to the plane averaging is defined as

$$f' = f - \langle f \rangle. \tag{13}$$

Based on previous study [39], the present computational domain size, the number of runs for each case, and the grid resolution are appropriate in terms of both accuracy and convergence for performing DNS of wind turbulence over breaking waves.
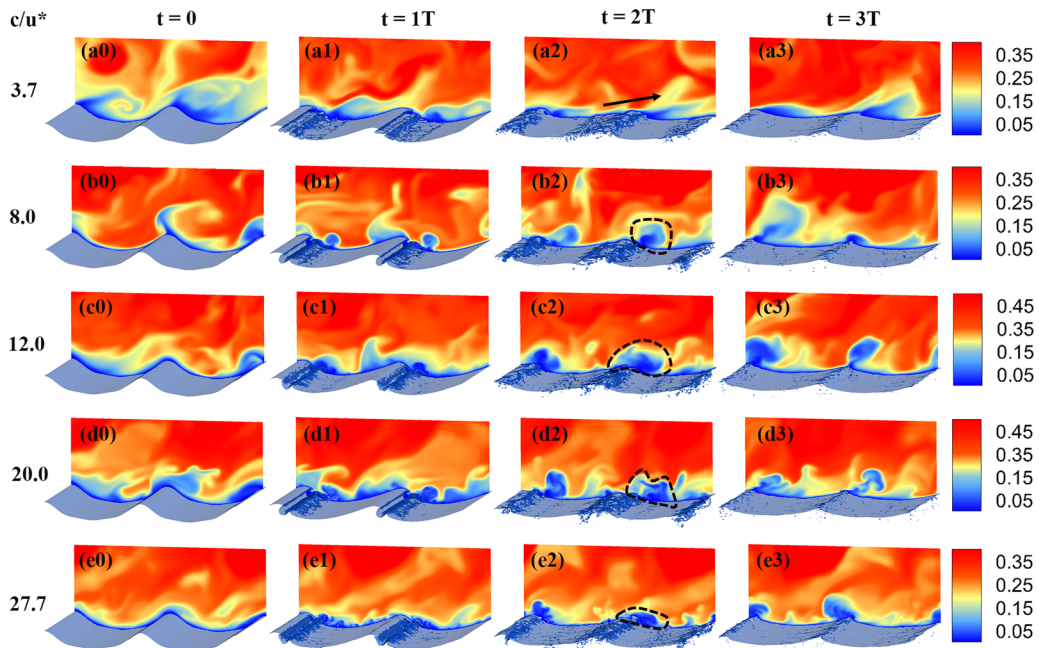
FIG. 2. Instantaneous snapshots of the geometry of breaking waves and contours of temperature on an x-z plane in cases with different wave ages. At $t = 2T$, the arrow in the first row indicates the direction of the separated airflow over the wave crest of a slow wave. Dotted circles in subsequent rows outline the cold region induced by the ejection of cold air during wave breaking.

IV. RESULTS

A. Instantaneous wave geometries and temperature fields

Figure 2 shows successive snapshots of the wave geometries and temperature fields. The results of different wave ages are shown in different rows. At $t = 0$, the initial wave geometries for the five cases remain the same [Figs. 2(a0)–2(e0)]. As the wave evolves, the wave crest forms an overturning jet and impinges onto the water surface at $t = T$ [Figs. 2(a1)–2(e1)]. After the first plunging event at $t = 2T$, the interface geometries become more complex [Figs. 2(a2)–2(e2)]. The simulations are stopped at $t = 3T$ when the wave breaking calms down [Figs. 2(a3)–2(e3)]. In the literature, the wave-breaking process has been studied through both numerical simulations [39,40,96] and experimental measurements [15–18]. The interface geometries shown in Fig. 2 are consistent with the previous studies (see Supplemental Material for details of the evolution of temperature and wave interface [97]).

The evolution of instantaneous temperature fields in different cases is visualized using contours in an x-z plane in Fig. 2. It is observed that the temperature at $t = 3T$ is significantly higher in the top row with a wave age of $c/u^* = 3.7$, compared to the initial stage at $t = 0$. Conversely, in other cases, the temperature at $t = 3T$ is comparable to or lower than that at $t = 0$. In the top row, cold air in the wave trough lifts upward due to airflow separation (indicated by the arrow). In the other rows, cold air is ejected upward by the wave motion during wave breaking, forming a circular region of cold air above the wave crest (indicated by circles at $t = 2T$). This observation suggests that the temperature increase in the smallest wave age case is caused by turbulence mixing, which brings hot air from above to lower elevations when the wave flattens after breaking. In contrast, the temperature decrease in other wave age cases is associated with the ejection of cold air. Interestingly, the decrease in temperature in the largest wave age case is less significant than that in cases with intermediate
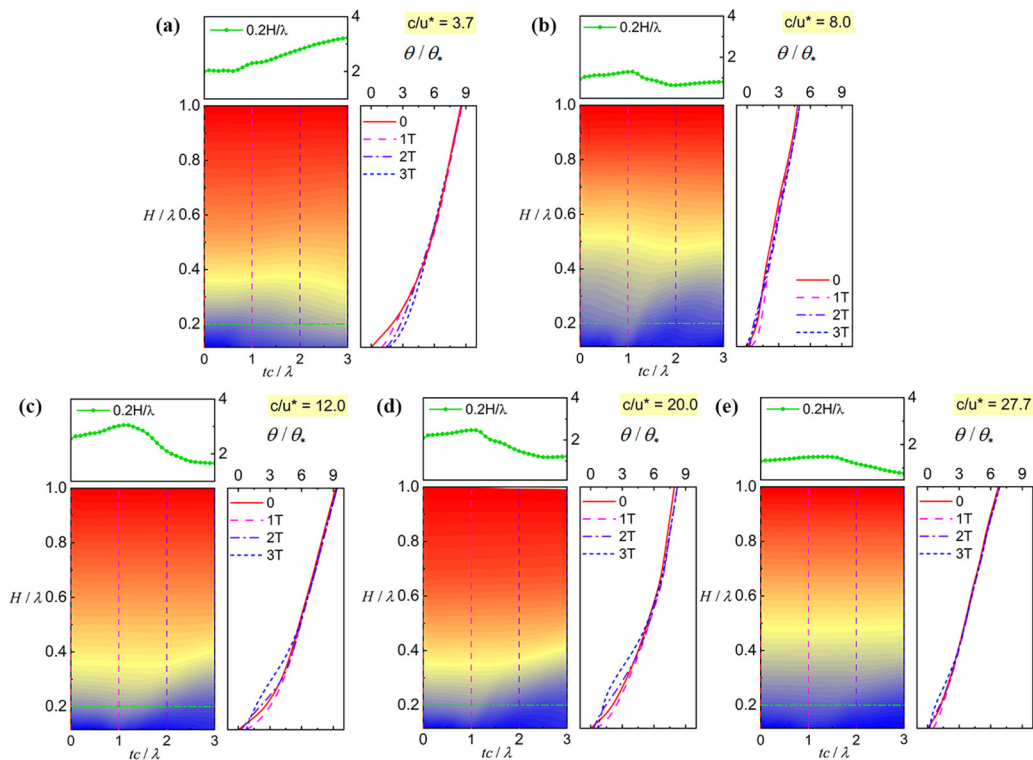
FIG. 3. Time evolution of the plane-averaged mean temperature $\langle\theta\rangle/\theta_*$ for different wave age cases. (a) $c/u^* = 3.7$, (b) $c/u^* = 8.0$, (c) $c/u^* = 12.0$, (d) $c/u^* = 20.0$, and (e) $c/u^* = 27.7$. To facilitate straightforward comparison across cases, the initial value of $\langle\theta\rangle$ at $z = 0.115\lambda$ in each case serves as the reference temperature. The temperature evolution at $H/\lambda = 0.2$ (green line) and the vertical profiles of temperature at different time instances are plotted for comparison purposes.

wave age, while the wave motion is stronger in the largest wave age case. This phenomenon is the subject of this study.

B. Plane-averaged statistics

1. Plane-averaged mean temperature

To quantify the effect of wave breaking on the temperature field, the evolution of the plane-averaged mean temperature $\langle\theta\rangle/\theta_*$ in different cases is compared in Fig. 3, where $\theta_* = (\alpha/u_*)(d\langle\theta\rangle/dz)$ is the friction temperature at the top boundary $z = 2\lambda$. We choose the x-y plane at $z = 0.115\lambda$ as a reference, which is slightly higher than the initial wave crest, to conduct the plane averaging above it. Thus, the vertical profiles of $\langle\theta\rangle/\theta_*$ start from $z = 0.115\lambda$. The plane-averaged quantities are not defined below this plane to avoid the air-water mixed region. The heat transfer below the wave crest can be investigated through phase averaging as in Sec. IV C. Because the temperature is treated as a passive scalar, its absolute value is not associated with the momentum transport. It is common to examine its relative value with respect to a reference temperature. To facilitate a straightforward comparison of the results for different cases, the initial value of $\langle\theta\rangle$ at $z = 0.115\lambda$ in each case is set as the reference temperature, i.e., $\langle\theta\rangle_{z=0.115\lambda,\,t=0} = 0$.

Figure 3(a) illustrates that $\langle\theta\rangle/\theta_*$ increases with time in the case with the youngest wave age ($c/u^* = 3.7$) in the near-wave region ($H/\lambda < 0.5$). From Figs. 3(b)–3(e), it is observed that the temperature increases until approximately $t \approx T$ and then decreases in cases with larger wave

TABLE II. Velocity and temperature variations between $t = 3T$ and $t = 0$ in the near-wave region for different cases.

$c/u*$	3.7	8.0	12.0	20.0	27.7
$\Delta\langle u \rangle$	0.797	1.154	0.701	1.497	0.798
$\Delta\langle \theta \rangle$	0.627	0.0148	-0.584	-0.574	-0.230

ages. As a result, the temperature $\langle\theta\rangle/\theta_*$ at $t = 3T$ is lower than its initial value. Additionally, the temperature decrement in the cases with wave ages of $c/u^* = 8.0$ [Fig. 3(b)] and $c/u^* = 27.7$ [Fig. 3(e)] is relatively smaller than that in the cases with wave ages of $c/u^* = 12.0$ [Fig. 3(c)] and $c/u^* = 20.0$ [Fig. 3(d)]. These observations of temperature evolution highlight the complexity of wave age effects on heat transfer during wave breaking in a nonmonotonic way.

To quantify the bulk effect of wave breaking on temperature field, we define the following temperature variation between the mean temperature at $t = 3T$ and $t = 0$ in the near-wave region:

$$\Delta\langle\theta\rangle = \frac{1}{0.5\lambda - 0.115\lambda}\int_{0.115\lambda}^{0.5\lambda}(\langle\theta\rangle|_{t=3T} - \langle\theta\rangle|_{t=0})dz. \quad (14)$$

It is evident from Fig. 3 that $\Delta\langle\theta\rangle$ is nonmonotonic in response to the increase in the wave age. The values of $\Delta\langle\theta\rangle$ in different cases are listed in Table II. To compare the effects of wave breaking on the temperature and velocity, Table II also lists the values of $\Delta\langle u\rangle$, which is defined similar to $\Delta\langle\theta\rangle$ in Eq. (14), with θ replaced by u. Table II shows that, as the wave age increases, $\Delta\langle\theta\rangle$ initially changes its sign from $\Delta\langle\theta\rangle_{c/u^*=3.7}/\theta_* = 0.627$ to $\Delta\langle\theta\rangle_{c/u^*=12.0}/\theta_* = -0.584$, and subsequently decreases to a smaller negative value of $\Delta\langle\theta\rangle_{c/u^*=27.7}/\theta_* = -0.230$ as the wave age further increases. Such a nonmonotonic variation is not observed for the mean velocity. As noted by Yang *et al.* [39], the mean velocity increases after wave breaking at all wave ages. This point is also evident from Table II showing that the value of $\Delta\langle u\rangle$ is positive in all cases. This contrast between the mean temperature and mean velocity indicates that the temperature responds in a more complex manner than the velocity to breaking waves at different wave ages. It should be noted that the temperature profiles at $t = 0$ in Fig. 3 correspond to a statistically stationary state, and thus the temperature variation $\Delta\langle\theta\rangle$ between $t = 0$ and $3T$ purely reflects the effect of wave breaking. In the following content, we further investigate the mechanism underlying the nonmonotonic behavior of the mean temperature variation with respect to the wave age through the analyses of temperature fluctuation fluxes.

2. Plane-averaged temperature fluctuation fluxes

The temperature fluctuation flux $-\langle\theta'w'\rangle$ is crucial for the evolution of the mean temperature. This point is evident from the following transport equation of the mean temperature:

$$\frac{\partial\langle\theta\rangle}{\partial t} = -\frac{\partial\langle\theta'w'\rangle}{\partial z} + \alpha\frac{\partial^2\langle\theta\rangle}{\partial z^2}. \quad (15)$$

Recalling the definition of turbulence statistics in Sec. III C, the temperature fluctuation flux $-\langle\theta'w'\rangle$ can be further decomposed into a wave-coherent part $-\langle\tilde{\theta}\tilde{w}\rangle$ and a turbulence-induced part $-\langle\theta''w''\rangle$ as

$$-\langle\theta'w'\rangle = -\langle\tilde{\theta}\tilde{w}\rangle - \langle\theta''w''\rangle. \quad (16)$$

Figures 4–6 respectively depict the time evolution of $-\langle\theta'w'\rangle$, $-\langle\tilde{\theta}\tilde{w}\rangle$, and $-\langle\theta''w''\rangle$ among five cases. In Fig. 4, to facilitate a straightforward visualization of the time evolution of temperature fluctuation in the turbulent active region, the figure shows $-\langle\theta'w'\rangle$ at $H/\lambda = 0.2$ ($y^+ \approx 30$). Additionally, the vertical profiles of $-\langle\theta'w'\rangle$ at four representative time instants ($t = 0, T, 2T$, and $3T$) are presented, with arrows indicating the trend of temperature change. According to Eq. (15),
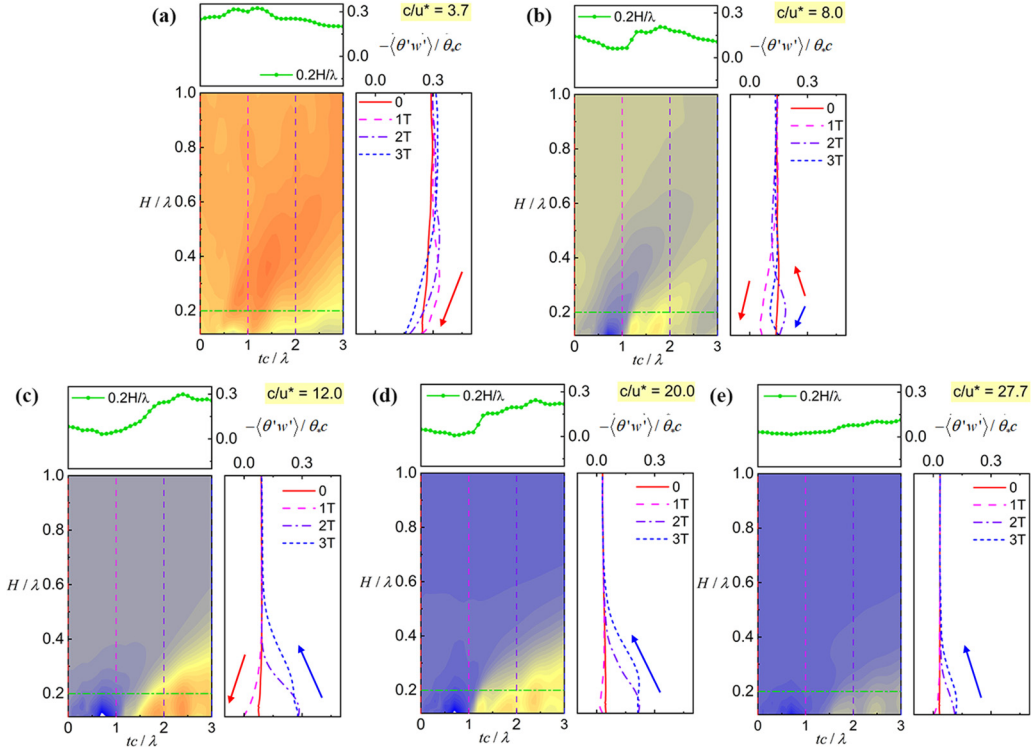
FIG. 4. Time evolution of the plane-averaged total temperature fluctuation flux $-\langle\theta'w'\rangle/\theta_*c$ for different wave age cases: (a) $c/u^* = 3.7$, (b) $c/u^* = 8.0$, (c) $c/u^* = 12.0$, (d) $c/u^* = 20.0$, and (e) $c/u^* = 27.7$. The evolution of $-\langle\theta'w'\rangle/\theta_*c$ at $H/\lambda = 0.2$ (green line) and the vertical profiles of $-\langle\theta'w'\rangle/\theta_*c$ at different time instances are also shown for comparison purposes. The arrow direction in the vertical profiles suggests the transport direction of the mean temperature induced by the temperature fluctuation fluxes.

the heat tends to be transported from a high-flux region to a low-flux region. Specifically, positive flux gradient [i.e., $-\partial\langle\theta'w'\rangle/\partial z > 0$] corresponds to downward transport of heat, resulting in the increase of temperature in that region (note that the mean temperature increases with the altitude), and is denoted using a downward red arrow. When $-\partial\langle\theta'w'\rangle/\partial z$ is negatively valued, an upward blue arrow is used to indicate the decrease of temperature in that region.

It is observed from Fig. 4(a) that in the youngest wave age case, the total temperature fluctuation flux $-\langle\theta'w'\rangle/\theta_*c$ is approximately a vertical straight line at $t = 0$. When the overturning jet impinges onto the water interface at $t = T$, a peak occurs in the profile of $-\langle\theta'w'\rangle$ at $z/\lambda = 0.3$. This peak leads to an increasing and decreasing effect in the mean temperature below and above it, respectively. After the first plunging event at $t = 2T$, this peak moves upward gradually. As a result, the region with the temperature increment expands to higher altitudes [see Fig. 3(a)]. The consistency in the contributions of $-\langle\theta'w'\rangle$ and $-\langle\theta''w''\rangle$ [see Figs. 4(a) and 6(a)] to the evolution of mean temperature indicates that, over slow breaking waves, the heat transfer is dominated by turbulence. It is observed from Fig. 4(b) that the peak of the total temperature fluctuation flux $-\langle\theta'w'\rangle/\theta_*c$ at $t = T$ does not appear in the case with a wave age of $c/u_* = 8.0$. Instead, an overall negatively valued gradient of $-\langle\theta'w'\rangle$ indicates an increase in mean temperature near the water surface. Following the first plunging event at $t = 2T$, the peak emerges at $z/\lambda = 0.2$, suggesting temperature mixing near the turbulent active region. The negatively valued peak of $-\langle\theta'w'\rangle/\theta_*c$ at $t = 3T$ compensates for the mixing effect at $t = 2T$, resulting in an imperceptible change in the plane-averaged mean temperature $\langle\theta\rangle/\theta_*$ after wave breaking.
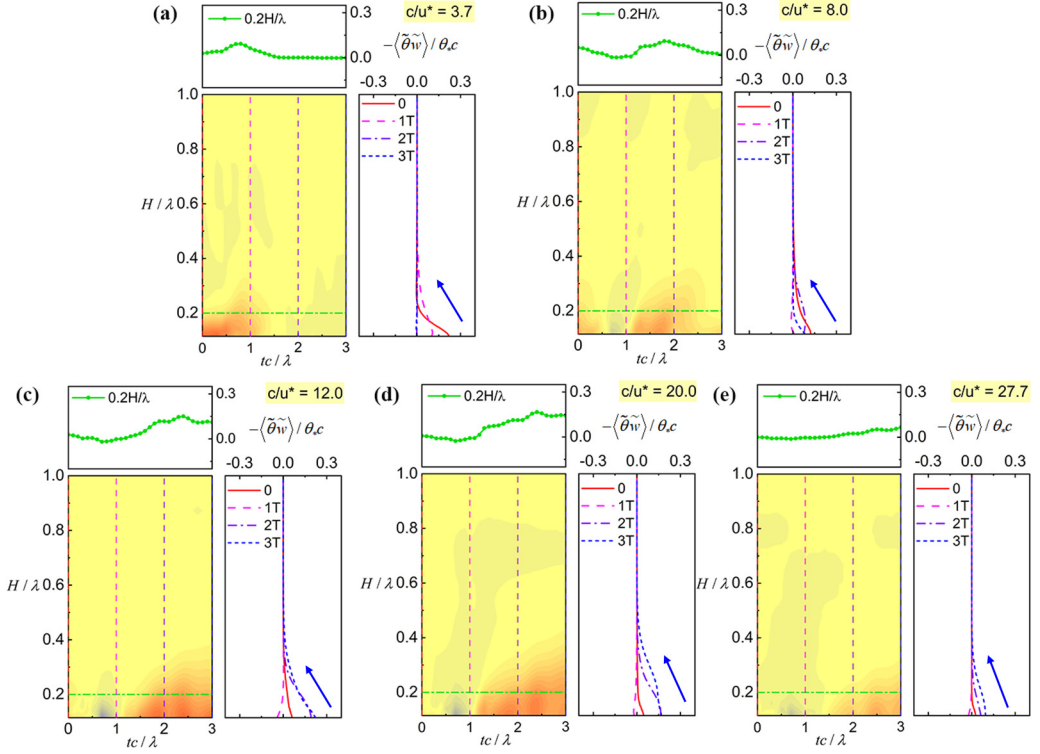
FIG. 5. Time evolution of the plane-averaged wave-induced flux $-\langle\tilde{\theta}\tilde{w}\rangle/\theta_* c$ for different wave age cases: (a) $c/u^* = 3.7$, (b) $c/u^* = 8.0$, (c) $c/u^* = 12.0$, (d) $c/u^* = 20.0$, and (e) $c/u^* = 27.7$. The evolution of $-\langle\tilde{\theta}\tilde{w}\rangle/\theta_* c$ at $H/\lambda = 0.2$ (green line) and the vertical profiles of $-\langle\tilde{\theta}\tilde{w}\rangle/\theta_* c$ at different time instances are also shown for comparison purposes. The meaning of the red and blue arrows are the same as in Fig. 4.

From Fig. 4(c), it is seen that for the case with a wave age of $c/u_* = 12.0$, the gradient of $-\langle\theta'w'\rangle$ is positively valued at $t = T$, indicating a slight increase in the mean temperature near the water surface. At $t = 2T$, $-\langle\theta'w'\rangle$ is drastically enhanced near the water surface, leading to a decreasing effect on the mean temperature in this region. From $t = 2T$ to $t = 3T$, the region with negative gradients of $-\langle\theta'w'\rangle$ expands to a higher altitude, indicating a decrease in temperature over a larger area. In the cases with $c/u_* = 20.0$ and $c/u_* = 27.7$, as observed from Figs. 4(d) and 4(e), $-\langle\theta'w'\rangle$ experiences a similar evolution process as in the case with a wave age of $c/u_* = 12.0$. A comparison among Figs. 4(c)–4(e) shows that the gradients of $-\langle\theta'w'\rangle$ are significantly larger in the cases with wave ages of $c/u_* = 12.0$ and $c/u_* = 20.0$ than the case with a wave age of $c/u_* = 27.7$. Consequently, the temperature decrement in the cases with wave ages of $c/u_* = 12.0$ and $c/u_* = 20.0$ is more significant. However, this reason alone is insufficient to explain why the temperature decrease occurs over a wider region in these two cases [see the comparison among Figs. 3(c)–3(e)].

To analyze this observation, it is noted from Figs. 5 and 6 that, in the cases with wave ages of $c/u_* = 12.0$ and $c/u_* = 20.0$, the magnitude of $-\langle\tilde{\theta}\tilde{w}\rangle$ is smaller than that of $-\langle\theta''w''\rangle$ above $z = 0.35\lambda$. This result suggests that the temperature decrease in the region away from the wave surface is dominated by turbulent motions in both wave cases. Additionally, Fig. 6 shows that the magnitude of $-\langle\theta''w''\rangle$ is negligible in the case with the largest wave age compared to that in the cases with wave ages of $c/u_* = 12.0$ and $c/u_* = 20.0$. Particularly in the cases with wave ages of $c/u_* = 12.0$ and $c/u_* = 20.0$, after the peak in the profile of $-\langle\theta''w''\rangle$ occurs at $t = 2T$, the peak magnitude is further amplified from $t = 2T$ to $t = 3T$. This evidence suggests that the presence of nonlinear interaction
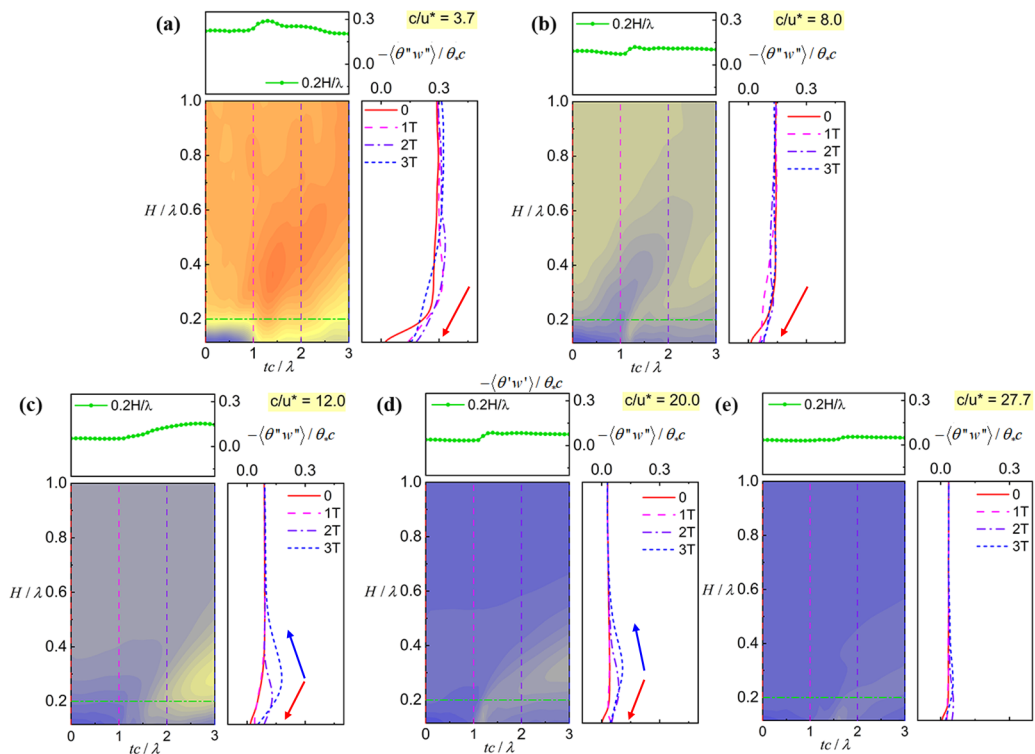
FIG. 6. Time evolution of the plane-averaged turbulence-induced flux $-\langle\theta''w''\rangle/\theta_*c$ for different wave age cases: (a) $c/u^* = 3.7$, (b) $c/u^* = 8.0$, (c) $c/u^* = 12.0$, (d) $c/u^* = 20.0$, and (e) $c/u^* = 27.7$. The evolution of $-\langle\theta''w''\rangle/\theta_*c$ at $H/\lambda = 0.2$ (green line) and the vertical profiles of $-\langle\theta''w''\rangle/\theta_*c$ at different time instances are also shown for comparison purposes. The meaning of the red and blue arrows are the same as in Fig. 4.

between turbulence-induced and wave-coherent dynamics enhances the vertical turbulence-induced temperature flux after the first plunging event in the cases with wave ages of $c/u_* = 12.0$ and $c/u_* = 20.0$, which is nevertheless absent in the case with the largest wave age. This nonlinear interaction is the key process leading to a more significant decrement of mean temperature in the intermediate wave age case than in the largest wave age case.

Thus far, we observe that the evolution of temperature fluctuation fluxes is highly correlated with the wave age and can be classified through the wave-breaking stage. For the case with small wave age, i.e., the young wave, represented by the wave age of $c/u_* = 3.7$, the turbulence-induced temperature fluctuation fluxes are dominant, resulting in the increase in temperature. For the case with wave age $c/u_* = 12.0$, i.e., the intermediate wave, both turbulence-induced and wave-induced temperature fluctuation fluxes contribute to the decrease in temperature. For the old wave stage represented by the case of $c/u_* = 27.7$, the wave-induced temperature fluctuation fluxes make primary contribution to the temperature decrease in a small elevation range near the wave surface.

C. Phase-averaged statistics

1. Phase-averaged vertical temperature fluctuation fluxes

To further investigate the effect of wave age on the heat transport above breaking waves, it is useful to examine the variation of the phase-averaged statistics in an x-z plane. For the sake of conciseness, the remainder of this paper focuses on presenting results for $c/u^* = 3.7$, $c/u^* = 12.0$, and $c/u^* = 27.7$ to demonstrate the effect of wave age on the temperature. This selection is justified as these values represent three primary wind-wave development stages, namely, the young,
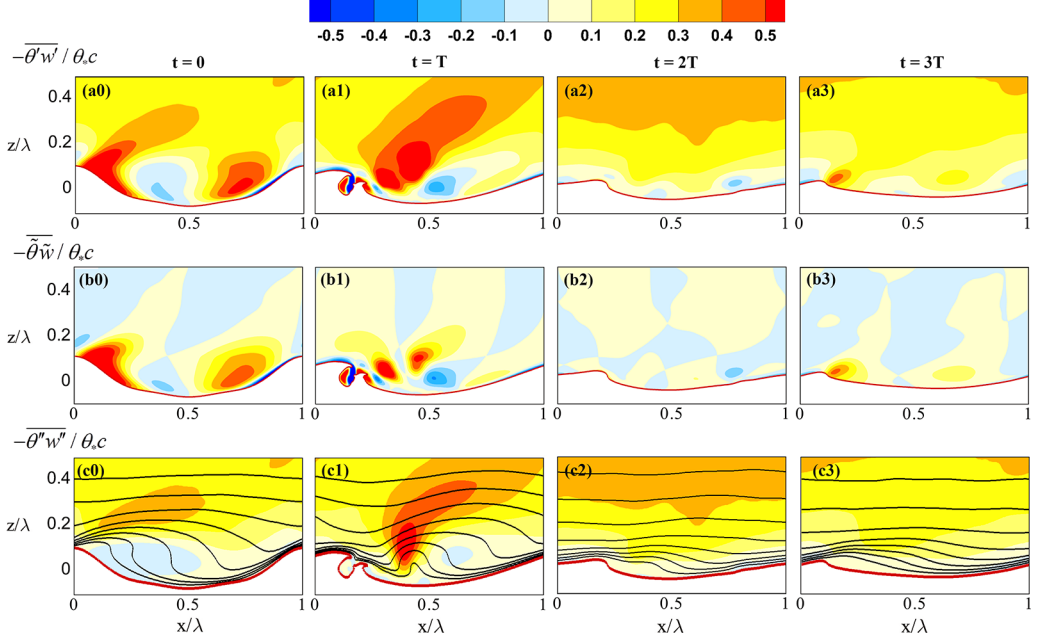
FIG. 7. Phase-averaged temperature fluctuation fluxes at different time instants for the slow wave case with $c/u_* = 3.7$. [(a0)–(a3)] $-\overline{\theta' w'}/\theta_* c$, [(b0)–(b3)] $-\overline{\tilde{\theta} \tilde{w}}/\theta_* c$, and [(c0)–(c3)] $-\overline{\theta'' w''}/\theta_* c$ at [(a0)–(c0)] $t = 0$, [(a1)–(c1)] $t = T$, [(a2)–(c2)] $t = 2T$, and [(a3)–(c3)] $t = 3T$.

intermediate, and old wave stages. Additionally, the results above show that the temperature fluctuation flux evolution in these three wave age cases is representative among the five cases. The analyses start with the contours of phase-averaged vertical temperature fluctuation fluxes. The results for cases with slow wave ($c/u_* = 3.7$), intermediate wave ($c/u_* = 12.0$), and fast wave ($c/u_* = 27.7$) are displayed in Figs. 7–9, respectively. In all figures, the upper row, middle row, and lower row show the total flux $-\overline{\theta' w'}$, its wave-coherent part $-\overline{\tilde{\theta} \tilde{w}}$, and the turbulence-induced part $-\overline{\theta'' w''}$, respectively. From left to right, the four columns show the results at $t = 0, T, 2T$, and $3T$, respectively. All fluxes are nondimensionalized using $\theta_* c$.

By comparing the total flux with its wave-coherent and turbulence-induced parts shown in Fig. 7, it is evident that, in the slow wave case ($c/u_* = 3.7$), the wave-coherent part influences the total flux only in a small vicinity region of the water surface. For example, as shown in Figs. 7(a0) and 7(b0), the maxima of both the total flux $-\overline{\theta' w'}$ and its wave-coherent part $-\overline{\tilde{\theta} \tilde{w}}$ occur above the leeward face of the wave before wave breaking. Above $z/\lambda = 0.3$, the distribution of the total flux is in general consistent with that of the turbulence-induced part $-\overline{\theta'' w''}$. Specifically, the wave breaking leads to the magnitude increment of both $-\overline{\theta' w'}$ and $-\overline{\theta'' w''}$ above $z/\lambda = 0.3$. This observation is consistent with the plane-averaged fluxes $-\langle \theta' w' \rangle$ and $-\langle \theta'' w'' \rangle$ shown in Figs. 4(a) and 6(a), respectively. The above results show that, in the slow wave case, the temperature is primarily influenced by wind turbulence, while the effect of wave motion becomes negligible after wave breaking.

In the intermediate wave case ($c/u_* = 12.0$), as shown in Figs. 8(a0) and 8(a1), the total flux $-\overline{\theta' w'}$ is intense near the wave surface before the wave plunging takes place at $t = T$. It is evidently dominated by the wave-coherent part shown in Figs. 8(b0) and 8(b1). After the wave plunging ($t \geqslant 2T$), the upward wave-coherent motion [see the streamlines of the wave-coherent velocity ($\tilde{u}$, $\tilde{w}$) shown in Figs. 8(b2) and 8(b3)] delivers cold air near the water surface to a higher altitude, generating a large magnitude of $-\overline{\tilde{\theta} \tilde{w}}$ above the leeward face of the wave below $z/\lambda = 0.3$. The
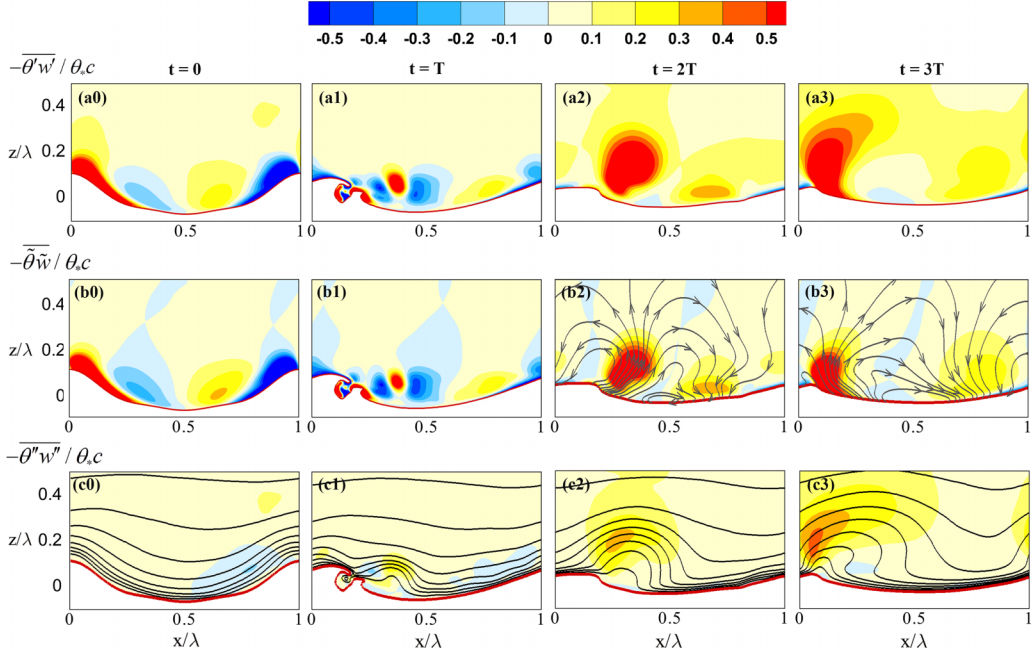
FIG. 8. Phase-averaged temperature fluctuation fluxes at different time instants for the intermediate wave case with $c/u_* = 12.0$. [(a0)–(a3)] $-\overline{\theta'w'}/\theta_*c$, [(b0)–(b3)] $-\overline{\tilde{\theta}\tilde{w}}/\theta_*c$, and [(c0)–(c3)] $-\overline{\theta''w''}/\theta_*c$ at [(a0)–(c0)] $t = 0$, [(a1)–(c1)] $t = T$, [(a2)–(c2)] $t = 2T$, and [(a3)–(c3)] $t = 3T$. The streamlines in panels (b2) and (b3) show the wave-coherent velocity $(\tilde{u}, \tilde{w})$. The black lines in panels (c0)–(c3) are the isopleths of $\bar{\theta}/\theta_*$.

total flux in this region also increases significantly. Compared to the wave-coherent flux, the total flux with a large magnitude reaches a higher altitude at $t = 3T$. The total flux at the high altitude is mainly influenced by the turbulence-induced flux, as shown in Fig. 8(c3). The above observations in the intermediate wave case indicate that both the air turbulence and wave motion have a significant effect on the temperature fluctuation flux. In other words, the comparable wind and wave motions synergistically contribute to the temperature decrement.

In the fast wave case ($c/u_* = 27.7$), the upward motion of airflow after wave plunging also induces a large magnitude of wave-coherent flux $-\overline{\tilde{\theta}\tilde{w}}$ and total flux $-\overline{\theta'w'}$, as observed from Figs. 9(a2), 9(a3), 9(b2), and 9(b3). This process is similar to the intermediate wave case described above. However, by comparing Figs. 8(c2) and 8(c3) with Figs. 9(c2) and 9(c3), it is observed that the turbulence-induced flux $-\overline{\theta''w''}$ is less intense in the fast wave case than that in the intermediate wave case. As a result, the total flux $-\overline{\theta'w'}$ does not reach a higher altitude in the fast wave case as it does in the intermediate wave case. The above findings in the fast wave case suggest that strong wave motion only affects the temperature in the vicinity of the wave surface when air turbulence is weak.

To further investigate the physical process generating the large magnitude of turbulence-induced flux $-\overline{\theta''w''}$ in the intermediate wave case, the isopleths of phase-averaged temperature $\bar{\theta}$ are superimposed in the lower panels of Figs. 8 and 9. From Figs. 8(c2) and 8(c3), it is observed that the isopleths of $\bar{\theta}$ are compressed above the leeward face of the wave due to the upward motion of the airflow. This means that the temperature gradient is large in this region. The large magnitude of the turbulence-induced flux $-\overline{\theta''w''}$ also occurs in this region, indicating that the gradient of wave-coherent temperature $\tilde{\theta}$ [note that the gradient of phase-averaged temperature $\bar{\theta}$ in the x direction is determined by its wave-coherent part based on Eq. (12)] and the vertical turbulence-induced flux $-\overline{\theta''w''}$ are correlated to some extent. In contrast, it is observed from
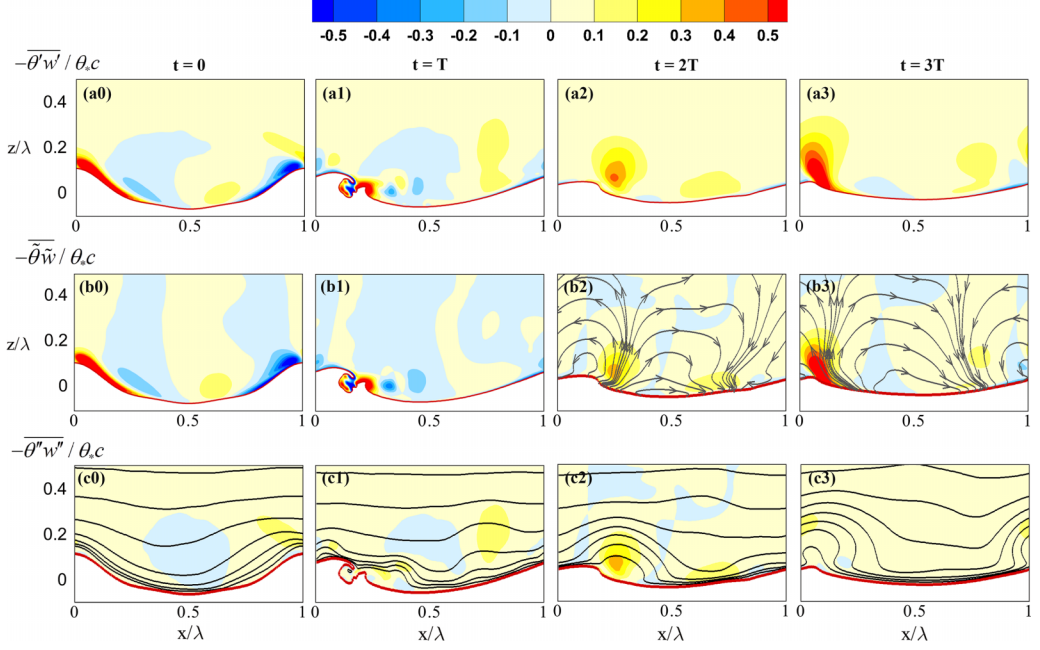
FIG. 9. Phase-averaged temperature fluctuation fluxes at different time instants for the fast wave case with $c/u_* = 27.7$. [(a0)–(a3)] $-\overline{\theta' w'}/\theta_* c$, [(b0)–(b3)] $-\overline{\tilde{\theta}\tilde{w}}/\theta_* c$, and [(c0)–(c3)] $-\overline{\theta'' w''}/\theta_* c$ at [(a0)–(c0)] $t = 0$, [(a1)–(c1)] $t = T$, [(a2)–(c2)] $t = 2T$, and [(a3)–(c3)] $t = 3T$. The streamlines in panels (b2) and (b3) show the wave-coherent velocity $(\tilde{u}, \tilde{w})$. The black lines in panels (c0)–(c3) are the isopleths of $\bar{\theta}/\theta_*$.

Fig. 9(c3) that the temperature isopleths are also compressed in the fast wave case, but $-\overline{\theta'' w''}$ is not significantly enhanced. The above comparison between the intermediate wave and fast wave cases indicates that the strong turbulence-induced flux $-\overline{\theta'' w''}$ in the intermediate wave case is produced by a complex chain of physical processes.

2. Production of $-\overline{\theta'' w''}$

To elucidate the mechanism underlying the large magnitude of the vertical turbulence-induced temperature flux $-\overline{\theta'' w''}$ in the intermediate wave case ($c/u_* = 12.0$), we examine the production term of its transport equation. The transport equation of $-\overline{\theta'' u_i''}$ is expressed as [98]

$$\frac{D(-\overline{\theta'' u_i''})}{Dt} = \overline{u_i'' u_k''}\frac{\partial \bar{\theta}}{\partial x_k} + \overline{u_k'' \theta''}\frac{\partial \bar{u}_i}{\partial x_k} + \frac{\partial(\overline{u_i'' u_k'' \theta''})}{\partial x_k} - \frac{\partial}{\partial x_k}\left(\overline{\theta''\frac{\partial u_i''}{\partial x_k}} + \frac{1}{\mathrm{Pr}}\overline{u_i''\frac{\partial \theta''}{\partial x_k}}\right)$$
$$+ \overline{\theta''\frac{\partial p''}{\partial x_i}} + \left(1 + \frac{1}{\mathrm{Pr}}\right)\overline{\frac{\partial u_i''}{\partial x_k}\frac{\partial \theta''}{\partial x_k}}. \tag{17}$$

The first two terms on the right-hand side of Eq. (17) are the production term, which quantifies a fast reaction of the temperature fluctuation flux to the change in the mean temperature $\bar{\theta}$ and mean velocity $\bar{u}_i$. Given the conditions $\langle w \rangle = 0$ and $\partial\langle\theta\rangle/\partial x = 0$, the production term for $-\overline{\theta'' w''}$ can be simplified to

$$P_{-\overline{\theta'' w''}} = \overline{\theta'' u_i''}\frac{\partial \bar{w}}{\partial x_i} + \overline{w'' u_i''}\frac{\partial \bar{\theta}}{\partial x_i}. \tag{18}$$

By applying the decomposition given by Eq. (12), the above production term can be decomposed into five parts as

$$P_{-\overline{\theta'' w''}} = \sum_{i=1}^{5} P_{-\overline{\theta'' w''}}^{(i)}, \tag{19}$$

where $P_{-\overline{\theta'' w''}}^{(i)}$ for $i = 1$–5 are written as

$$P_{-\overline{\theta'' w''}}^{(1)} = \overline{\theta'' u''} \frac{\partial \tilde{w}}{\partial x}, \tag{20}$$

$$P_{-\overline{\theta'' w''}}^{(2)} = \overline{\theta'' w''} \frac{\partial \tilde{w}}{\partial z}, \tag{21}$$

$$P_{-\overline{\theta'' w''}}^{(3)} = \overline{u'' w''} \frac{\partial \tilde{\theta}}{\partial x}, \tag{22}$$

$$P_{-\overline{\theta'' w''}}^{(4)} = \overline{w'' w''} \frac{\partial \tilde{\theta}}{\partial z}, \tag{23}$$

$$P_{-\overline{\theta'' w''}}^{(5)} = \overline{w'' w''} \frac{\partial \langle \theta \rangle}{\partial z}. \tag{24}$$

It is understood from the analyses in Sec. IV C that, in the intermediate wave case, the generation of the strong vertical turbulence-induced flux $-\overline{\theta'' w''}$ initiates near $z/\lambda = 0.2$ at approximately $t = 2T$ [see Fig. 8(b2)]. Therefore, we compare the streamwise variation of its production terms at $z/\lambda = 0.2$ and $t = 2T$ for different cases in Fig. 10.

As shown in Fig. 10(a), the total production $P_{-\overline{\theta'' w''}}$ in the slow wave case is relatively large with a minimum value above the wave crest. Thus, the turbulence-induced temperature fluctuation flux $-\overline{\theta'' w''}$ is larger in the case with a slow wave than in other cases. In the cases with intermediate and fast waves, the horizontal profile of $P_{-\overline{\theta'' w''}}$ is similar. A peak of $P_{-\overline{\theta'' w''}}$ is observed approximately at $x/\lambda = 0.25$, where the wave crest is located (see Figs. 8 and 9). The peak value of $P_{-\overline{\theta'' w''}}$ in the fast wave case is smaller than that in the intermediate wave case. As a result, the turbulence-induced flux $-\overline{\theta'' w''}$ is stronger in the intermediate wave case than in the fast wave case.

Among the five parts of the production term [Eqs. (19)–(24)], $P_{-\overline{\theta'' w''}}^{(2)}$ and $P_{-\overline{\theta'' w''}}^{(3)}$ are relatively small. In the slow wave case, $P_{-\overline{\theta'' w''}}^{(5)}$ makes dominant contributions to the total production. In the intermediate wave case, $P_{-\overline{\theta'' w''}}^{(1)}$ is larger than $P_{-\overline{\theta'' w''}}^{(4)}$ and $P_{-\overline{\theta'' w''}}^{(5)}$, and it is deduced to be the key process that is responsible for the large magnitude of the vertical turbulence-induced temperature fluctuation flux $-\overline{\theta'' w''}$ in the intermediate wave case. This process is, however, absent in the fast wave case as evidenced by the small magnitude of $P_{-\overline{\theta'' w''}}^{(1)}$ shown in Fig. 10(b).

To further reveal the reason for the occurrence of a large magnitude of $P_{-\overline{\theta'' w''}}^{(1)}$ in the intermediate wave case, we examine $-\overline{\theta'' u''}$ and $\partial \tilde{w}/\partial x$ at $t = 2T$ separately, visualized in Fig. 11 using color contours and isopleths. As shown, in the slow wave case, the magnitude of $-\overline{\theta'' u''}$ is negative above the wave crest, and the velocity gradient $\partial \tilde{w}/\partial x$ has a small positive value. Thus, it cannot provide a positive $P_{-\overline{\theta'' w''}}^{(1)}$. In the intermediate wave case, negatively valued flux $-\overline{\theta'' u''}$ overlaps with the positive velocity gradient $\partial \tilde{w}/\partial x$ above the wave crest around $(x/\lambda, z/\lambda) = (0.25, 0.2)$, leading to a positive production term $P_{-\overline{\theta'' w''}}^{(1)}$ there. In the fast wave case, a positive velocity gradient occurs at the same location, but the flux $-\overline{\theta'' u''}$ is of small negative value or even positive there. As a result, the production term $P_{-\overline{\theta'' w''}}^{(1)}$ is significantly smaller in the fast wave case than in the intermediate wave case. Based on the above observation, we further investigate the mechanism underlying the production of $-\overline{\theta'' u''}$ in the following section.
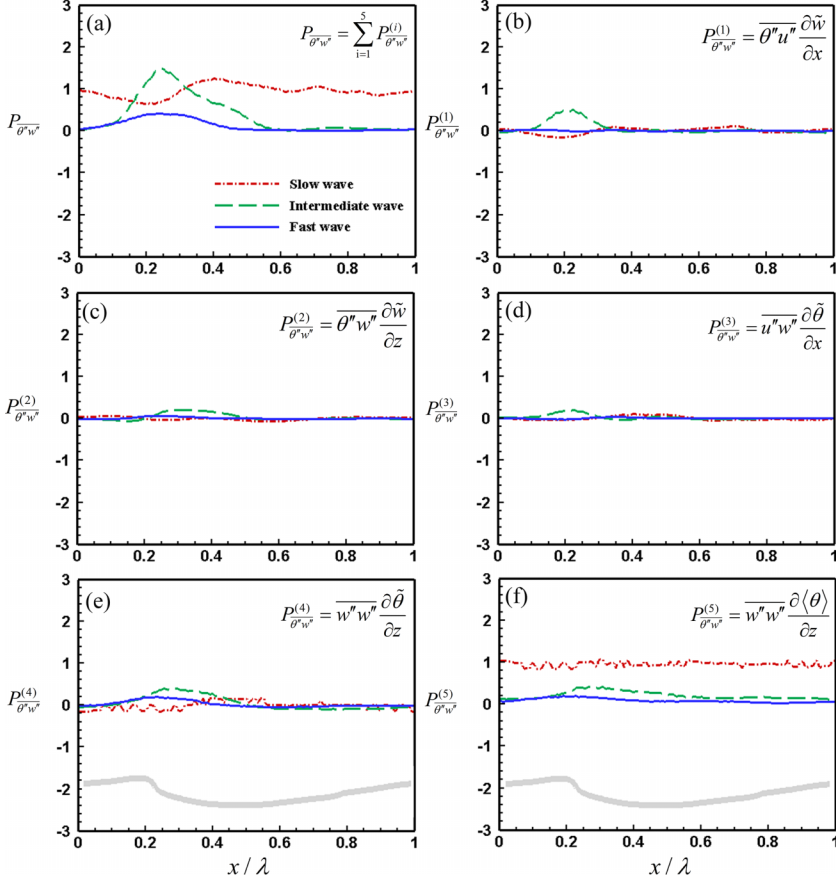
FIG. 10. Profiles of the production term and its five parts in the transport equation of $-\overline{\theta''w''}$ [Eqs. (19)–(24)] along the x direction at $z/\lambda = 0.2$ and $t = 2T$ in different cases. All production terms are nondimensionalized by $\theta_* c^2/\lambda$. The thick gray line in panels (e) and (f) shows the geometry of the phase-averaged wave interface at $t = 2T$.

3. Production of $-\overline{\theta''u''}$

The production term in the transport equation of $-\overline{\theta''u''}$ is written as

$$P_{-\overline{\theta''u''}} = \overline{\theta''u_i''}\frac{\partial \overline{u}}{\partial x_i} + \overline{u''u_i''}\frac{\partial \overline{\theta}}{\partial x_i}. \tag{25}$$

Similar to the above analyses on the production term of $-\overline{\theta''w''}$, $P_{-\overline{\theta''u''}}$ is decomposed into six parts as

$$P = \sum_{i=1}^{6} P_{-\overline{\theta''u''}}^{(i)}. \tag{26}$$

The expressions of $P_{-\overline{\theta''u''}}^{(1)-(6)}$ are given as follows:

$$P_{-\overline{\theta''u''}}^{(1)} = \overline{\theta''u''}\frac{\partial \tilde{u}}{\partial x}, \tag{27}$$

$$P_{-\overline{\theta''u''}}^{(2)} = \overline{\theta''w''}\frac{\partial \tilde{u}}{\partial z}, \tag{28}$$
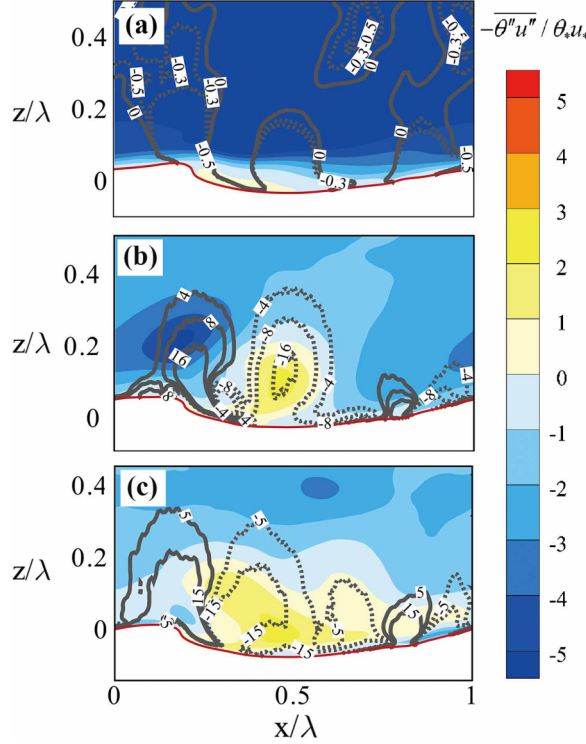
FIG. 11. Phase-averaged turbulence-induced streamwise temperature flux $-\overline{\theta''u''}/\theta_* c$ at $t = 2T$ for the cases with (a) slow wave, (b) intermediate wave, and (c) fast wave. The isopleths of $\tilde{w}$ are superimposed, with solid and dashed lines representing positive and negative values, respectively.

$$P^{(3)}_{-\overline{\theta''u''}} = \overline{\theta''w''}\frac{\partial \langle u \rangle}{\partial z}, \tag{29}$$

$$P^{(4)}_{-\overline{\theta''u''}} = \overline{u''u''}\frac{\partial \tilde{\theta}}{\partial x}, \tag{30}$$

$$P^{(5)}_{-\overline{\theta''u''}} = \overline{u''w''}\frac{\partial \tilde{\theta}}{\partial z}, \tag{31}$$

$$P^{(6)}_{-\overline{\theta''u''}} = \overline{u''w''}\frac{\partial \langle \theta \rangle}{\partial z}, \tag{32}$$

where $\partial \langle u \rangle/\partial x = 0$ and $\partial \langle \theta \rangle/\partial x = 0$ are applied.

Figure 12 compares the streamwise variation of the total production term $P_{-\overline{\theta''u''}}$ and its six parts for different wave ages. The results at $z/\lambda = 0.2$ and $t = 2T$ are shown. Unlike the vertical flux $-\overline{\theta''w''}$, the production of the streamwise flux $-\overline{\theta''u''}$ is significantly smaller in the slow wave case than in the cases with intermediate and fast waves. In the intermediate wave case, the negative total production term observed from Fig. 12(a) imposes a gain effect on the negatively valued streamwise turbulence-induced flux $-\overline{\theta''u''}$ there [see Fig. 11(b)], while the positive total production in the fast wave case [Fig. 12(a)] tends to suppress the negatively valued $-\overline{\theta''u''}$. As a result, the magnitude of $-\overline{\theta''u''}$ is larger in the fast wave case than in the intermediate wave case [see Figs. 11(b) and 11(c)].

In the intermediate wave case, $P^{(4)}_{-\overline{\theta''u''}}$ makes the primary contribution to the total production among all six parts, followed by $P^{(3)}_{-\overline{\theta''u''}}$ and $P^{(5)}_{-\overline{\theta''u''}}$. From its definition given by Eq. (30), it can be
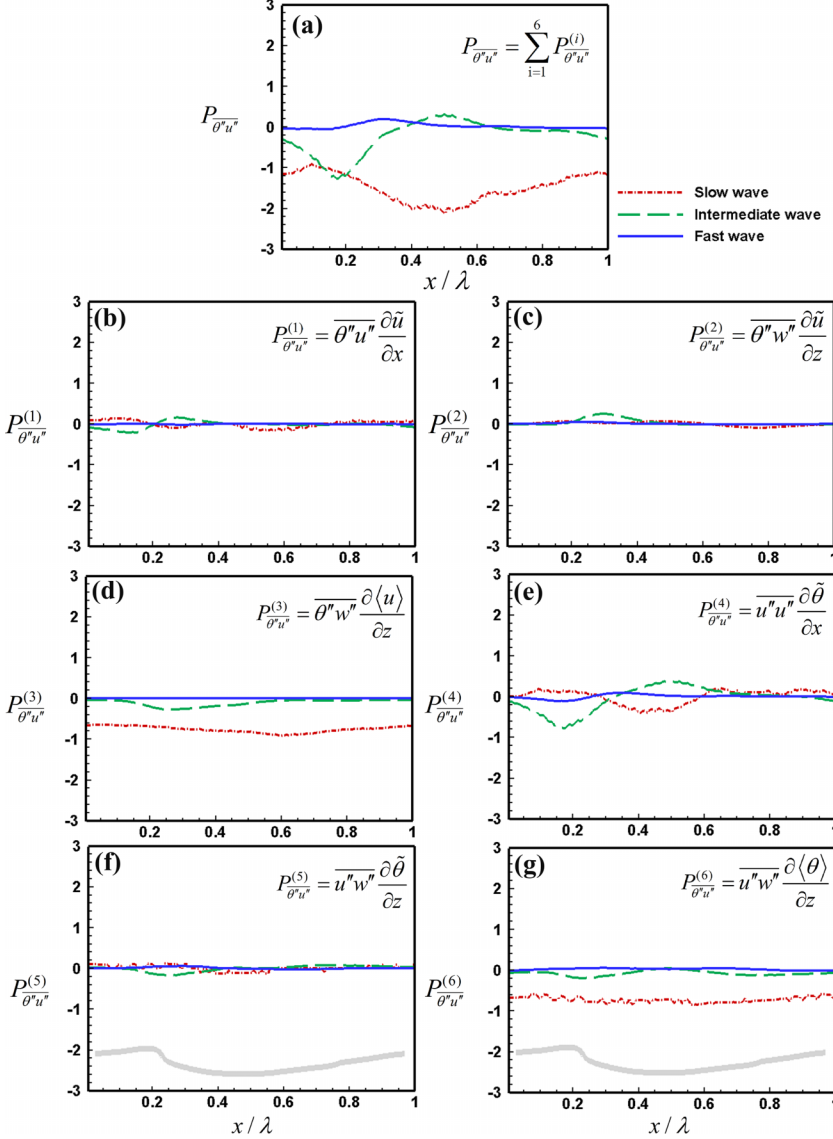
FIG. 12. Profiles of the production terms in the transport equation of $-\overline{\theta''u''}$ along the x direction at $z/\lambda = 0.2$ and $t = 2T$ in different cases. All production terms are nondimensionalized by $\theta_* c^2/\lambda$. The thick gray line in panels (f) and (g) shows the geometry of the phase-averaged wave interface at $t = 2T$.

recognized that $P^{(4)}_{-\overline{\theta''u''}}$ is correlated to the streamwise gradient of the wave-coherent temperature, $\partial\tilde{\theta}/\partial x$, which is induced by the upward wave-coherent velocity generated during wave plunging [Figs. 8(b2), 8(b3), 8(c2), and 8(c3)]. This result indicates that the generation of $-\overline{\theta''u''}$ originates from wave-coherent motions. In the fast wave case, the magnitude of $P^{(4)}_{-\overline{\theta''u''}}$ is smaller than that in the intermediate wave case. As a result, negative $-\overline{\theta''u''}$ does not occur in the fast wave case.

Thus far, the mechanism underlying the temperature decrement in the intermediate wave case is clear. Briefly speaking, this is caused by a joint effect of both wave-coherent and turbulence-induced dynamics. To be specific, in the intermediate wave case, the wave-coherent motion first induces a wave-coherent temperature gradient $\partial\tilde{\theta}/\partial x$ [Figs. 8(b2), 8(b3), 8(c2), and 8(c3)], which interacts

with the streamwise turbulent temperature fluctuation $\overline{u''u''}$ to produce streamwise temperature flux $-\overline{\theta''u''}$ [Fig. 12(e)]. The interaction between $-\overline{\theta''u''}$ and the wave-coherent vertical velocity gradient $\partial\tilde{w}/\partial x$ further generates the vertical turbulent temperature flux $-\overline{\theta''w''}$ (Fig. 8, bottom row), which, together with the wave-coherent flux $-\overline{\tilde{\theta}\tilde{w}}$ (Fig. 8, middle row), leads to the decrease in the mean temperature $\langle\theta\rangle$. In the slow wave case, the above process is absent, because the wave-coherent motion is weak and thus the turbulence-induced flux dominates the whole process (Fig. 7, bottom row). In the fast wave case, although the wave-coherent motion is strong (Fig. 9, middle row), its interaction with the turbulence-induced motion is absent. The physical process converting the wave-coherent temperature $\tilde{\theta}$ into the streamwise turbulent temperature flux $-\overline{\theta''u''}$ is broken in the slow and fast wave cases (see Fig. 12). This is because the characteristic velocity scales of wave-coherent and turbulence-induced motions as represented respectively by the wave phase speed c and wind friction velocity u_* are distinctly separated at the large and slow wave ages, such that they are not coupled as tightly as in the intermediate wave case. As a result, it is more difficult for the energy to be transported between these two processes. We note that our present relatively low Reynolds number DNS data cannot be directly compared with measured data. This is because the velocity and temperature boundary layers in real-world problems are thinner than those obtained from our DNS data, leading to an overestimation of the heat transfer coefficient. Therefore, we are not attempting to directly connect our findings to bulk coefficients. Instead, our objective is to understand the influence of wave motion on sensible heat flux within this complex system and to highlight the importance of incorporating the wave age effect in future prediction models. High Reynolds number simulation that includes turbulent models is a direction worth exploring in future work.

V. CONCLUSIONS

In this paper, the heat transfer in wind turbulence over breaking waves is studied using DNS. The air-water coupled system is solved on an Eulerian grid with the interface between the two fluid phases captured by the CLSVOF method. Five simulation cases with different wave ages are conducted to examine the effect of wave age on heat transfer.

From the simulation results, it is discovered that the wave age imposes a nonmonotonic effect on the air temperature variation in the wave-breaking process. In the slow wave case, the temperature near the wave surface increases after the wave breaking calms down. In the intermediate wave case, the temperature decreases after wave breaking. In the fast wave case, the temperature also decreases, but the decrement magnitude is smaller than that in the intermediate wave case.

The nonmonotonic response of the mean temperature to the wave age is investigated through the analyses of the temperature fluctuation fluxes. A joint effect of the wave-coherent and turbulence-induced temperature fluxes is found to be responsible for the temperature decrement in the air above the intermediate wave. Over the slow wave with small wave age, the effect of wave-coherent flux is negligible. Over the fast wave with large wave age, the turbulence-induced flux is weak due to the absence of a production process, which is attributed to the separation between the characteristic velocity scales of the wave-coherent and turbulence-induced dynamics.

As a final remark of this paper, we note that the temperature responds in a more complex manner to the wave age than the velocity does, in a sense that the mean streamwise velocity increases after wave breaking at all wave ages [39]. The finding of the present study indicates that it is crucial to consider the effect of wave age on the temperature fluxes associated with breaking waves by capturing the above dynamics in air-sea interaction models in future studies.

[1] T. Hara and S. E. Belcher, Wind profile and drag coefficient over mature ocean surface wave spectra, J. Phys. Oceanogr. **34**, 2345 (2004).

[2] B. K. Haus, D. Jeong, M. A. Donelan, J. A. Zhang, and I. Savelyev, Relative rates of sea-air heat transfer and frictional drag in very high winds, Geophys. Res. Lett. **37**, 2009GL042206 (2010).

[3] T. Hara and P. P. Sullivan, Wave boundary layer turbulence over surface waves in a strongly forced condition, J. Phys. Oceanogr. **45**, 868 (2015).

[4] M. L. Banner and D. H. Peregrine, Wave breaking in deep water, Annu. Rev. Fluid Mech. **25**, 373 (1993).

[5] W. E. Asher, A. T. Jessup, and M. A. Atmane, Oceanic application of the active controlled flux technique for measuring air-sea transfer velocities of heat and gases, J. Geophys. Res. **109**, 2003JC001862 (2004).

[6] C. J. Zappa, W. E. Asher, A. T. Jessup, J. Klinke, and S. R. Long, Microbreaking and the enhancement of air-water transfer velocity, J. Geophys. Res. **109**, 2003JC001897 (2004).

[7] J. T. Dawe and L. Thompson, Effect of ocean surface currents on wind stress, heat flux, and wind power input to the ocean, Geophys. Res. Lett. **33**, 2006GL025784 (2006).

[8] J. A. Mueller and F. Veron, Bulk formulation of the heat and water vapor fluxes at the air-sea interface, including nonmolecular contributions, J. Atmos. Sci. **67**, 234 (2010).

[9] S. Komori, K. Iwano, N. Takagaki, R. Onishi, R. Kurose, K. Takahashi, and N. Suzuki, Laboratory measurements of heat transfer and drag coefficients at extremely high wind speeds, J. Phys. Oceanogr. **48**, 959 (2018).

[10] D. H. Richter, A. E. Dempsey, and P. P. Sullivan, Turbulent transport of spray droplets in the vicinity of moving surface waves, J. Phys. Oceanogr. **49**, 1789 (2019).

[11] W. K. Melville, The role of surface-wave breaking in air-sea interaction, Annu. Rev. Fluid Mech. **28**, 279 (1996).

[12] M. Perlin and W. W. Schultz, Capillary effects on surface waves, Annu. Rev. Fluid Mech. **32**, 241 (2000).

[13] K. T. Kiger and J. H. Duncan, Air-entrainment mechanisms in plunging jets and breaking waves, Annu. Rev. Fluid Mech. **44**, 563 (2012).

[14] M. Perlin, W. Choi, and Z. Tian, Breaking waves in deep and intermediate waters, Annu. Rev. Fluid Mech. **45**, 115 (2013).

[15] J. H. Duncan, An experimental investigation of breaking waves produced by a towed hydrofoil, Proc. R. Soc. London A **377**, 331 (1981).

[16] S. E. Ramberg and O. M. Griffin, Laboratory study of steep and breaking deep water waves, J. Waterway, Port, Coastal, Ocean Eng. **113**, 493 (1987).

[17] P. Bonmarin, Geometric properties of deep-water breaking waves, J. Fluid Mech. **209**, 405 (1989).

[18] W. K. Melville, F. Veron, and C. J. White, The velocity field under breaking waves: Coherent structures and turbulence, J. Fluid Mech. **454**, 203 (2002).

[19] R. Gómez-ledesma, K. T. Kiger, and J. H. Duncan, The impact of a translating plunging jet on a pool of the same liquid, J. Fluid Mech. **680**, 5 (2011).

[20] D. H. Peregrine, Breaking waves on beaches, Annu. Rev. Fluid Mech. **15**, 149 (1983).

[21] P. Stansell and C. MacFarlane, Experimental investigation of wave breaking criteria based on wave phase speeds, J. Phys. Oceanogr. **32**, 1269 (2002).

[22] M. L. Banner and W. L. Peirson, Wave breaking onset and strength for two-dimensional deep-water wave groups, J. Fluid Mech. **585**, 93 (2007).

[23] M. P. Tulin and T. Waseda, Laboratory observations of wave group evolution, including breaking effects, J. Fluid Mech. **378**, 197 (1999).

[24] A. Babanin, D. Chalikov, I. Young, and I. Savelyev, Predicting the breaking onset of surface water waves, Geophys. Res. Lett. **34**, 2006GL029135 (2007).

[25] M. Perlin, J. He, and L. P. Bernal, An experimental study of deep water plunging breakers, Phys. Fluids **8**, 2365 (1996).

[26] K.-A. Chang and P. L.-F. Liu, Velocity, acceleration and vorticity under a breaking wave, Phys. Fluids **10**, 327 (1998).

[27] W. W. Schultz, J. Huh, and O. M. Griffin, Potential energy in steep and breaking waves, J. Fluid Mech. **278**, 201 (1994).

[28] M. L. Banner and X. Tian, On the determination of the onset of breaking for modulating surface gravity water waves, J. Fluid Mech. **367**, 107 (1998).

[29] J. B. Song and M. L. Banner, On determining the onset and strength of breaking for deep water waves. Part I: Unforced irrotational wave groups, J. Phys. Oceanogr. **32**, 2541 (2002).

[30] M. Derakhti, M. L. Banner, and J. T. Kirby, Predicting the breaking strength of gravity water waves in deep and intermediate depth, J. Fluid Mech. **848**, R2 (2018).

[31] M. Derakhti, J. T. Kirby, M. L. Banner, S. T. Grilli, and J. Thomson, A unified breaking onset criterion for surface gravity water waves in arbitrary depth, J. Geophys. Res. **125**, e2019JC015886 (2020).

[32] Z. Tian, M. Perlin, and W. Choi, Energy dissipation in two-dimensional unsteady plunging breakers and an eddy viscosity model, J. Fluid Mech. **655**, 217 (2010).

[33] A. Iafrati, Energy dissipation mechanisms in wave breaking processes: Spilling and highly aerated plunging breaking events, J. Geophys. Res. **116**, C07024 (2011).

[34] E. Meza, J. Zhang, and R. J. Seymour, Free-wave energy dissipation in experimental breaking waves, J. Phys. Oceanogr. **30**, 2404 (2000).

[35] H.-H. Hwung, W.-S. Chiang, and S.-C. Hsiao, Observations on the evolution of wave modulation, Proc. R. Soc. A **463**, 85 (2007).

[36] G. Chen, C. Kharif, S. Zaleski, and J. Li, Two-dimensional Navier-Stokes simulation of breaking waves, Phys. Fluids **11**, 121 (1999).

[37] A. Iafrati, Numerical study of the effects of the breaking intensity on wave breaking flows, J. Fluid Mech. **622**, 371 (2009).

[38] L. Deike, S. Popinet, and W. K. Melville, Capillary effects on wave breaking, J. Fluid Mech. **769**, 541 (2015).

[39] Z. Yang, B.-Q. Deng, and L. Shen, Direct numerical simulation of wind turbulence over breaking waves, J. Fluid Mech. **850**, 120 (2018).

[40] W. H. R. Chan, P. L. Johnson, P. Moin, and J. Urzay, The turbulent bubble break-up cascade. Part 2. Numerical simulations of breaking waves, J. Fluid Mech. **912**, A43 (2021).

[41] Q. Gao, G. B. Deane, and L. Shen, Bubble production by air filament and cavity breakup in plunging breaking wave crests, J. Fluid Mech. **929**, A44 (2021).

[42] C. A. Friehe and K. F. Schmitt, Parameterization of air–sea interface fluxes of sensible heat and moisture by the bulk aerodynamic formulas, J. Phys. Oceanogr. **6**, 801 (1976).

[43] W. G. Large and S. Pond, Sensible and latent heat flux measurements over the ocean, J. Phys. Oceanogr. **12**, 464 (1982).

[44] J. DeCosmo, K. B. Katsaros, S. D. Smith, R. J. Anderson, W. A. Oost, K. Bumke, and H. Chadwick, Air-sea exchange of water vapor and sensible heat: The Humidity Exchange Over the Sea (HEXOS) results, J. Geophys. Res. **101**, 12001 (1996).

[45] R. Pedreros, G. Dardier, H. Dupuis, H. C. Graber, W. M. Drennan, A. Weill, C. Guérin, and P. Nacass, Momentum and heat fluxes via the eddy correlation method on the R/V *L'Atalante* and an ASIS buoy, J. Geophys. Res. **108**, 2002JC001449 (2003).

[46] W. M. Drennan, J. A. Zhang, J. R. French, C. McCormick, and P. G. Black, Turbulent fluxes in the hurricane boundary layer. Part II: Latent heat flux, J. Atmos. Sci. **64**, 1103 (2007).

[47] F. J. Ocampo-Torres, M. A. Donelan, N. Merzi, and F. Jia, Laboratory measurements of mass transfer of carbon dioxide and water vapour for smooth and rough flow conditions, Tellus B **46**, 16 (1994).

[48] S. D. Smith, Coefficients for sea surface wind stress, heat flux, and wind profiles as a function of wind speed and temperature, J. Geophys. Res. **93**, 15467 (1988).

[49] C. W. Fairall, E. F. Bradley, D. P. Rogers, J. B. Edson, and G. S. Young, Bulk parameterization of air-sea fluxes for tropical ocean-global atmosphere coupled-ocean atmosphere response experiment, J. Geophys. Res. **101**, 3747 (1996).

[50] J.-J. Luo, S. Masson, S. Behera, S. Shingu, and T. Yamagata, Seasonal climate predictability in a coupled OAGCM using a different approach for ensemble forecasts, J. Clim. **18**, 4474 (2005).

[51] H. Kawamura, K. Ohsaka, H. Abe, and K. Yamamoto, DNS of turbulent heat transfer in channel flow with low to medium-high Prandtl number fluid, Int. J. Heat Fluid Flow **19**, 482 (1998).

[52] B. Debusschere and C. J. Rutland, Turbulent scalar transport mechanisms in plane channel and Couette flows, Int. J. Heat Mass Transf. **47**, 1771 (2004).

[53] S. Pirozzoli, M. Bernardini, and P. Orlandi, Passive scalars in turbulent channel flow at high Reynolds number, J. Fluid Mech. **788**, 614 (2016).

[54] J. Kim and P. Moin, Transport of passive scalars in a turbulent channel flow, in *Turbulent Shear Flows* (Springer, Berlin, 1989), Vol. 6, pp. 85–96.

[55] S. L. Lyons, T. J. Hanratty, and J. B. McLaughlin, Direct numerical simulation of passive heat transfer in a turbulent channel flow, Int. J. Heat Mass Transf. **34**, 1149 (1991).

[56] N. Kasagi, Y. Tomita, and A. Kuroda, Direct numerical simulation of passive scalar field in a turbulent channel flow, ASME J. Heat Mass Transfer **114**, 598 (1992).

[57] R. A. Antonia, H. Abe, and H. Kawamura, Analogy between velocity and scalar fields in a turbulent channel flow, J. Fluid Mech. **628**, 241 (2009).

[58] H. S. Choi and K. Suzuki, Large eddy simulation of turbulent flow and heat transfer in a channel with one wavy wall, Int. J. Heat Fluid Flow **26**, 681 (2005).

[59] T. S. Park, H. S. Choi, and K. Suzuki, Nonlinear k-ε-f_μ model and its application to the flow and heat transfer in a channel having one undulant wall, Int. J. Heat Mass Transfer **47**, 2403 (2004).

[60] S. Savino, G. Comini, and C. Nonino, Effect of corner angle on convection enhancement in wavy ducts with trapezoidal cross-sections, Int. J. Numer. Methods Fluids **44**, 885 (2004).

[61] A. Z. Dellil, A. Azzi, and B. A. Jubran, Turbulent flow and convective heat transfer in a wavy wall channel, Heat Mass Transfer **40**, 793 (2004).

[62] M. Mirzaei, A. Sohankar, L. Davidson, and F. Innings, Large eddy simulation of the flow and heat transfer in a half-corrugated channel with various wave amplitudes, Int. J. Heat Mass Transfer **76**, 432 (2014).

[63] P. P. Sullivan and J. C. McWilliams, Dynamics of winds and currents coupled to surface waves, Annu. Rev. Fluid Mech. **42**, 19 (2010).

[64] D. Yang and L. Shen, Direct-simulation-based study of turbulent flow over various waving boundaries, J. Fluid Mech. **650**, 131 (2010).

[65] M. P. Buckley and F. Veron, Structure of the airflow above surface waves, J. Phys. Oceanogr. **46**, 1377 (2016).

[66] D. Yang and L. Shen, Direct numerical simulation of scalar transport in turbulent flows over progressive surface waves, J. Fluid Mech. **819**, 58 (2017).

[67] T. Cao, B.-Q. Deng, and L. Shen, A simulation-based mechanistic study of turbulent wind blowing over opposing water waves, J. Fluid Mech. **901**, A27 (2020).

[68] L. Wang, W. Zhang, X. Hao, W.-X. Huang, L. Shen, C.-X. Xu, and Z. Zhang, Surface wave effects on energy transfer in overlying turbulent flow, J. Fluid Mech. **893**, A21 (2020).

[69] S. Banerjee, D. Lakehal, and M. Fulgosi, Surface divergence models for scalar exchange between turbulent streams, Int. J. Multiphase Flow **30**, 963 (2004).

[70] S. Komori, R. Kurose, K. Iwano, T. Ukai, and N. Suzuki, Direct numerical simulation of wind-driven turbulence and scalar transfer at sheared gas-liquid interfaces, J. Turbul. **11**, N32 (2010).

[71] W. Tsai, S. Chen, G. Lu, and C. S. Garbe, Characteristics of interfacial signatures on a wind-driven gravity-capillary wave, J. Geophys. Res. **118**, 1715 (2013).

[72] N. Takagaki, R. Kurose, Y. Tsujimoto, S. Komori, and K. Takahashi, Effects of turbulent eddies and Langmuir circulations on scalar transfer in a sheared wind-driven liquid flow, Phys. Fluids **27**, 016603 (2015).

[73] D. Lakehal, M. Fulgosi, G. Yadigaroglu, and S. Banerjee, Direct numerical simulation of turbulent heat transfer across a mobile, sheared gas-liquid interface, J. Heat Transfer **125**, 1129 (2003).

[74] A. T. Jessup, C. J. Zappa, M. R. Loewen, and V. Hesany, Infrared remote sensing of breaking waves, Nature (London) **385**, 52 (1997).

[75] S. Vagle, J. Gemmrich, and H. Czerski, Reduced upper ocean turbulence and changes to bubble size distributions during large downward heat flux events, J. Geophys. Res. **117**, 2011JC007308 (2012).

[76] G. B. Deane, D. Stokes, and A. H. Callaghan, Turbulence in breaking waves, Phys. Today **69**(10), 86 (2016).

[77] D. H. Richter and F. Veron, Ocean spray: An outsized influence on weather and climate, Phys. Today **69**(11), 34 (2016).

[78] F. Veron, Ocean spray, Annu. Rev. Fluid Mech. **47**, 507 (2015).

[79] M. Uhlmann, Interface-resolved direct numerical simulation of vertical particulate channel flow in the turbulent regime, Phys. Fluids **20**, 053305 (2008).

[80] Z. Yang, M. Lu, and S. Wang, A robust solver for incompressible high-Reynolds-number two-fluid flows with high density contrast, J. Comput. Phys. **441**, 110474 (2021).

[81] M. Lu, Z. Yang, and G. He, A robust scheme for numerical simulation of heat transfer in two-fluid flows with high volumetric heat capacity contrasts, Int. J. Numer. Methods Heat Fluid Flow **33**, 570 (2023).

[82] M. Sussman and E.-G. Puckett, A coupled level set and volume-of-fluid method for computing 3D and axisymmetric incompressible two-phase flows, J. Comput. Phys. **162**, 301 (2000).

[83] Y. Liu, Numerical study of strong free surface flow and breaking waves, Ph.D. thesis, The Johns Hopkins University, 2013.

[84] H. Lamb, *Hydrodynamics* (Cambridge University Press, Cambridge, UK, 1932).

[85] R. J. Rapp and W. K. Melville, Laboratory measurements of deep-water breaking waves, Philos. Trans. R. Soc. A **331**, 735 (1990).

[86] Z. Tian, M. Perlin, and W. Choi, Evaluation of a deep-water wave breaking criterion, Phys. Fluids **20**, 066604 (2008).

[87] P. Lubin and S. Glockner, Numerical simulations of three-dimensional plunging breaking waves: Generation and evolution of aerated vortex filaments, J. Fluid Mech. **767**, 364 (2015).

[88] K. C. Kim and R. J. Adrian, Very large-scale motion in the outer layer, Phys. Fluids **11**, 417 (1999).

[89] M. Guala, S. E. Hommema, and R. J. Adrian, Large-scale and very-large-scale motions in turbulent pipe flow, J. Fluid Mech. **554**, 521 (2006).

[90] J. H. Lee and H. J. Sung, Very-large-scale motions in a turbulent boundary layer, J. Fluid Mech. **673**, 80 (2011).

[91] W.-Y. Zhang, W.-X. Huang, and C.-X. Xu, Very large-scale motions in turbulent flows over streamwise traveling wavy boundaries, Phys. Rev. Fluids **4**, 054601 (2019).

[92] M. Perlin, H. Lin, and C.-L. Ting, On parasitic capillary waves generated by steep gravity waves: An experimental investigation with spatial and temporal measurements, J. Fluid Mech. **255**, 597 (1993).

[93] X. Liu and J. H. Duncan, The effects of surfactants on spilling breaking waves, Nature (London) **421**, 520 (2003).

[94] X. Liu and J. H. Duncan, An experimental study of surfactant effects on spilling breakers, J. Fluid Mech. **567**, 433 (2006).

[95] G. Caulliez, Dissipation regimes for short wind waves, J. Geophys. Res. **118**, 672 (2013).

[96] Z. Wang, J. Yang, and F. Stern, High-fidelity simulations of bubble, droplet and spray formation in breaking waves, J. Fluid Mech. **792**, 307 (2016).

[97] See Supplemental Material at http://link.aps.org/supplemental/10.1103/PhysRevFluids.9.084606 for the evolution of temperature and wave interface for the three representative wave age cases.

[98] M. Kozuka, Y. Seki, and H. Kawamura, DNS of turbulent heat transfer in a channel flow with a high spatial resolution, Int. J. Heat Fluid Flow **30**, 514 (2009).